

# A Novel Method to Identify AGNs Based on Emission Line Excess and the Nature of Low-luminosity AGNs in the Sloan Digital Sky Survey

## I – A Novel Method

Masayuki Tanaka

*Institute for the Physics and Mathematics of the Universe, The University of Tokyo  
5-1-5 Kashiwanoha, Kashiwa-shi, Chiba 277-8583, Japan  
masayuki.tanaka@ipmu.jp*

(Received ; accepted )

### Abstract

We develop a novel technique to identify active galactic nuclei (AGNs) and study the nature of low-luminosity AGNs in the Sloan Digital Sky Survey. This is the first part of a series of papers and we develop a new, sensitive method to identify AGNs in this paper. An emission line luminosity in a spectrum is a sum of a star formation component and an AGN component (if present). We demonstrate that an accurate estimate of the star formation component can be achieved by fitting model spectra, generated with a recent stellar population synthesis code, to a continuum spectrum. By comparing the observed total line luminosity with that attributed to star formation, we can tell whether a galaxy host an AGN or not. We compare our method with the commonly used emission line diagnostics proposed by Baldwin et al. (1981; hereafter BPT). Our method recovers the same star formation/AGN classification as BPT for 85% of the strong emission line objects, which comprise 43% of our sample. A unique feature of our method is its sensitivity: it is applicable to 78% of the sample. We further make comparisons between our method and BPT using stacked spectra and selection in X-ray and radio wavelengths. We show that, while the method suffers from incompleteness and contamination as any AGN identification methods do, it is overall a sensitive method to identify AGNs. We emphasize that the method can be applied at high redshifts (up to  $z \sim 1.7$  with red-sensitive optical spectrograph) without making any a priori assumptions about host galaxy properties. Another unique feature of the method is that it allows us to subtract emission line luminosity due to star formation and extract intrinsic AGN luminosity. We will make a full use of these features to study the nature of low-luminosity AGNs in Paper-II.

**Key words:** galaxies: active — methods: data analysis — X-rays: galaxies — radio continuum: galaxies

## 1. Introduction

Since the seminal work by Seyfert (1943) on broad emission line properties of spiral nebulae, there has been a rapid advance in our understanding of active galactic nuclei (AGNs). A number of spectroscopic surveys of nuclei of nearby galaxies have been performed since then (e.g., Heckman 1980; Ho et al. 1995) and large surveys of the local universe such as the 2 degree field survey (Colless et al. 2003) and the Sloan Digital Sky Survey (SDSS; York et al. 2000) have characterized properties of AGNs with an unprecedented statistical accuracy (e.g., Kauffmann et al. 2003; Heckman et al. 2004; Kewley et al. 2006; Schawinski et al. 2007). The realization that black hole mass correlates with host galaxy properties such as bulge luminosity and mass (Kormendy & Richstone 1995; Magorrian et al. 1998; Ferrarese & Merritt 2000; Gebhardt et al. 2000) has triggered a lot of effort to link super-massive black hole growth with galaxy growth. Recent simulations of galaxy evolution seem to achieve some success in reproducing observed properties of galaxies by incorporating energy feedback from AGNs, although details of such a feedback mechanism are still fairly uncertain (Granato et al. 2004; Croton et al. 2006; Bower et al. 2006).

In order to perform an observational study of effects of AGNs on galaxy evolution, one first has to identify AGNs.

AGNs can be identified in a variety of ways at essentially all wavelengths (X-rays, mid-IR, and radio detections and optical emission line diagnostics). The energy source of AGN activity is the material accreting onto a central super-massive black hole that is heated to high temperature, traveling at high velocity. It is thought to be the source of X-ray emission due to the inverse-Compton scattering of thermal photons from the accretion disk off relativistic electrons. The surrounding dust torus is heated by the radiation, thus resulting in strong thermal emission at mid-IR wavelengths. In some cases, the central engine ejects jets perpendicular to the accretion disk and they are often observed in radio wavelengths due to the Synchrotron radiation. Also, the central engine ionizes the gas in the galaxy out to hundred-parsec to kilo-parsec scales. The ionization state of the surrounding gas is often higher than normal star forming regions, showing characteristic emission line intensity ratios. AGNs exhibit these unique spectral features and AGN identification methods aim at detecting them.

In this paper, we focus on optical emission line techniques. Baldwin et al. (1981) first presented a method to separate AGNs from star forming galaxies using flux ratios of four emission lines in the optical wavelengths ( $H\beta$ , [OIII],  $H\alpha$ , and [NII]). We refer to this diagnostics as BPT in what follows. AGNs and star forming galaxies form distinct sequences with some overlap on the BPT diagram. Theoretical calcu-

lations based on photo-ionization models have been made to understand the distribution on this diagram (e.g., Ho et al. 1993; Kewley et al. 2001; Stasińska et al. 2006). For instance, Kewley et al. (2001) performed detailed photo-ionization modeling over a range of ionization parameters and defined a region of the diagram where photo-ionization is unlikely due to stars. Massive spectroscopic surveys of the local universe such as the Sloan Digital Sky Survey (SDSS; York et al. 2000) revealed that star forming galaxies form a tight sequence on the BPT diagram, suggesting that the ionization state of star forming galaxies does not vary so widely as explored by Kewley et al. (2001). Kauffmann et al. (2003) empirically revised the theoretical curve of Kewley et al. (2001) using the data from SDSS and this is now a commonly used discriminator between AGNs and star forming galaxies.

Despite the popularity, however, the BPT diagnostics has disadvantages. Firstly, it requires four emission lines, which are not always easy to measure with sufficient signal-to-noise ratios. In particular,  $H\beta$  can be very weak in low-luminosity AGNs and it often limits the sensitivity of BPT. Secondly, it requires  $H\alpha$  and [NII]. These lines migrate to near-IR at  $z > 0.5$  and it is hard to measure these lines at high redshifts. Attempts have been made to overcome these issues by using emission lines that are observable even at  $z > 0.5$  or by making a priori assumption of host galaxy properties. Rola et al. (1997) suggested that [OII] and [NEIII] $\lambda\lambda 3869, 3968$  could help identify AGNs when  $H\alpha$  and [NII] are not available. Lamareille et al. (2004) showed that [OII]/ $H\beta$  can be used in place of [NII]/ $H\alpha$ . Yan et al. (2006) and Yan et al. (2011a) proposed ways to identify AGNs using a priori assumption about host galaxy properties. Recently, Juneau et al. (2011) presented a new diagnostics using [OIII]/ $H\beta$  and stellar mass of the hosts. In this paper, we make an attempt to overcome the issues with a new, physically motivated method to identify AGNs. In particular, we do not assume any host galaxy properties a priori as done in Yan et al. (2006, 2011) and Juneau et al. (2011) to identify AGNs. This is essential to study relationships between the AGN activity and host galaxy properties.

The structure of this paper is as follows. We develop a new method to identify AGNs in Section 2, followed by extensive tests of the method in Section 3. We summarize the strengths and weaknesses of the method and conclude the paper in Section 4. Nature of low-luminosity AGNs and their host galaxy properties will be presented in Paper-II. Unless otherwise stated, we adopt  $\Omega_M = 0.3$ ,  $\Omega_\Lambda = 0.7$ , and  $H_0 = 70 \text{ km s}^{-1} \text{ Mpc}^{-1}$ . All the magnitudes are given in the AB system. We use the following abbreviations : AGN for active galactic nucleus, BPT for the Baldwin et al. (1981) diagnostics, SF for star formation, and SFR for star formation rate. Emission lines used in this work include [OII]  $\lambda\lambda 3726, 3729$ ,  $H\beta$   $\lambda 4861$ , [OIII]  $\lambda 5007$ , [OI]  $\lambda 6300$ ,  $H\alpha$   $\lambda 6563$ , [NII]  $\lambda 6583$ , and [SII]  $\lambda 6716, 6730$ .

## 2. A new method

As mentioned in the last section, the commonly used emission line diagnostics involves intensity ratios of emission lines to identify a signature of AGN. An ionizing spectrum of AGN is typically harder than spectra of young stars, and thus AGNs

exhibit characteristic emission line intensity ratios. The most commonly adopted Baldwin et al. (1981) diagnostics involves four emission lines, which are not always easy to measure at high signal-to-noise. That hinders efficient identification of low-luminosity AGNs in surveys such as SDSS. However, one does not necessarily have to rely on ratios of emission lines. A single emission line in principle contains information about an underlying AGN. If a galaxy hosts an AGN, the emission line luminosity we observe originates both from star formation and AGN:

$$L_{measured} = L_{SF} + L_{AGN}, \quad (1)$$

where  $L_{SF}$  is an emission line luminosity due to star formation and  $L_{AGN}$  is a luminosity due to AGN. The idea behind our method is to estimate  $L_{SF}$  of a galaxy and compare it with  $L_{measured}$ . If we observe a significant luminosity excess in  $L_{measured}$ , it means that the galaxy shows a significant  $L_{AGN}$  and it likely hosts an AGN. In this section, we develop a method to estimate  $L_{SF}$  and quantify how accurate our  $L_{SF}$  is. Then we move on to perform an extensive test of our AGN identification method in the next section.

### 2.1. Sloan Digital Sky Survey

In this paper, we use data from the Sloan Digital Sky Survey Data Release 7 (Abazajian et al. 2009). The SDSS utilizes a dedicated 2.5m telescope installed at the Apache Point Observatory (Gunn et al. 2006) and the survey is in two parts: imaging and spectroscopy. The SDSS has imaged a quarter of the sky in five photometric bands (*urgiz*; Fukugita et al. 1996; Gunn et al. 1998; Doi et al. 2010) with unprecedented accuracy (Ivezić et al. 2007; Padmanabhan et al. 2008). The SDSS spectroscopic survey utilizes double fiber-fed spectrographs and obtains 640 spectra simultaneously covering a wavelength range of 3800Å to 9200Å with a resolving power of  $R \sim 2000$ . Each fiber subtends  $3''$  on the sky. The survey consists of 3 major components : main galaxy sample (Strauss et al. 2002), luminous red galaxy sample (Eisenstein et al. 2001), and QSO sample (Richards et al. 2002). The main sample is a flux-limited sample down to  $r = 17.77$  selected from the imaging survey and we use objects in the main sample in this paper.

We apply the following criteria to select galaxies for our study: SPECCLASS=2 (i.e., objects are galaxies) located at  $0.02 < z < 0.10$  with high confidence flags (ZCONF>0.8 and ZWARNING=0). We intentionally remove QSO-like objects (SPECCLASS=3) from the sample because our method is not applicable to those objects (as shown below, our method assumes that a continuum spectrum is dominated by stars, not by AGN). We have 283,031 objects in total, a quarter of which are identified as AGNs by the method developed in this paper. We correct the SDSS spectra for the Galactic extinction using the extinction curve of Cardelli et al. (1989) and the extinction map from Schlegel et al. (1998).

### 2.2. Spectral fitting

How do we estimate  $L_{SF}$  of an emission line? It has actually been a long standing issue in AGN studies. AGN emission is contaminated with star formation emission and that has often hindered detailed studies of intrinsic AGN output. We cannot use any emission lines to estimate  $L_{SF}$  because it is hard to

discriminate it from  $L_{AGN}$ . We have to rely on other available information. One might use a star formation indicator such as mid-IR emission to measure it, but one faces the same problem – it is difficult to disentangle  $L_{SF}$  and  $L_{AGN}$  in mid-IR. We take a novel approach to solve the problem. AGNs show strong emission lines, but their continuum emission is usually very weak in optical wavelengths, except for very strong AGNs and quasars (Binette et al. 1994). We use optical continuum emission of galaxies, which is dominated by stellar light, not by AGNs, to estimate  $L_{SF}$ . We fit observed spectra of galaxies with model spectral templates of galaxies with various star formation histories to obtain star formation rates (SFRs) and dust extinction. From these numbers, we can work out  $L_{SF}$ .

We generate model templates using an updated version of the Bruzual & Charlot (2003) code with improved treatment of thermally pulsating AGB stars. Free parameters in the models are

- **Star formation history:** We assume a simple, exponentially decaying star formation rate to describe star formation histories. The exponential time scale is allowed to vary between 0 (i.e., instantaneous burst) and  $\infty$  (i.e., constant star formation rate).
- **Dust extinction:** We use the two component extinction model of Charlot & Fall (2000). We adopt  $\mu = 0.3$ , which means that 30% of the extinction is due to the ambient interstellar medium, which affects all stars. The remaining 70% is due to dust in star forming regions, and it affects only stars younger than  $10^7$  yr. We modify the extinction curve of  $\tau \propto \lambda^{-0.7}$  to that of Cardelli et al. (1989), which is close to  $\tau \propto \lambda^{-1.0}$ . We justify the choice of the Cardelli et al. (1989) curve over the Charlot & Fall (2000) curve in the Appendix. We allow the optical depth in the  $V$ -band,  $\tau_V$ , to vary between 0 (i.e., no dust) and 3.
- **Metallicity:** We use the solar metallicity models only. If we include super-solar and sub-solar metallicity models, we introduce too much degeneracies between age, metallicity, and dust and degrade the fits. We justify the exclusion of non-solar metallicity models in the Appendix.
- **Age:** We apply a logical constraint that the age of a model template must be younger than the age of the universe at a given redshift. We do not use models with young ages with  $< 1$  Gyr. Due to the degeneracies between the above mentioned parameters, we can fit galaxies with very young models, but they often give inaccurate SFRs. The age limit of 1 Gyr removes most of such bad fits.

We assume the Chabrier initial mass function (Chabrier 2003). We fit the observed spectra of galaxies with these templates using the  $\chi^2$  statistics. We generate sets of the templates with varying stellar velocity dispersions ranging from 75 to 250  $\text{km s}^{-1}$  with a 25  $\text{km s}^{-1}$  step and fit the galaxies with the closest dispersion. We have  $\sim 8,400$  model templates in each set. In the fitting, we mask out regions around strong emission lines such as [OII], H $\beta$ , [OIII], H $\alpha$ , [NII], [SII], etc, because we want to fit the spectra of stars. In addition, we mask out a region around 5577Å, where a strong night-sky Oxygen line is located. The best-fitting models give SFRs, stellar mass, and

$\tau_V$ , which we will extensively use in our analysis. We derive an uncertainty on each parameter by taking  $\Delta\chi^2 = 1$  from the best fit. However, due to correlations between adjacent wavelength points of the SDSS spectra and also to strong degeneracies between the model parameters, the derived errors may not be accurate. We can empirically measure the errors in, e.g.,  $L_{SF}$  by comparing those from direct emission line measurements as shown below.

We subtract the best-fitting model spectra from the observed spectra to obtain continuum-subtracted spectra to measure emission line fluxes. As summarized by Tojeiro et al. (2011), population synthesis models are not always perfect and they under/over subtract the continuum in some wavelength regions. For example, in the case of Bruzual & Charlot (2003) model, it often over-subtracts the continuum around H $\beta$  (Asari et al. 2007). We therefore remove the residual continuum by median-filtering the spectra within a running box of  $\Delta\lambda = 60\text{Å}$ . We then simply sum the fluxes around an emission line to measure its flux within a wavelength range of  $|\lambda - \lambda_{line}| < 8\text{Å}$ . One could fit Gaussian to an emission line to measure the flux (e.g., Tremonti et al. 2004), but AGNs may well show narrow and broad components simultaneously. As AGNs are the focus of this work, we do not assume any line profiles. A fraction of galaxy light is missed from the 3 arcsec fiber. In order to correct for the missing light, we compute the slit loss by comparing  $r$ -band magnitude synthesized from the spectrum with the  $r$ -band Petrosian magnitude from imaging. The stellar masses and SFRs of the host galaxies are corrected for the slit losses and are indicated with a subscript *apercorr* in figures. Note that this is only a first-order correction because of the assumption employed here that the light in the fiber is representative of the entire galaxy light.

Strong AGNs often exhibit featureless continuum in the UV (e.g., Kinney et al. 1991), which might affect our spectral fitting and the resultant parameters. We have checked effects of such featureless continuum by including additional continuum flux in the form of  $F_\nu \propto \nu^{-1.5}$  (Schmitt et al. 1999) to the stellar spectra generated with the population synthesis code. The strength of the featureless continuum ranges from 0 to 30% of an observed spectrum at 5500Å with a step of 5%. We find that such a continuum decreases the accuracy of our spectral fits. For example, an accuracy of the predicted [OII]+[OIII] luminosity decreases to 0.35 dex (we obtain 0.24 dex without the continuum as shown below). Furthermore, the best-fitting models often give strong featureless continuum to star forming galaxies selected from BPT (i.e., non-AGNs). These results suggest that such a continuum just increases the degeneracies between the model parameters and does not improve the fits. It probably makes sense to include the featureless continuum in the fits to study strong AGNs, but for our purpose of studying low-luminosity AGNs, we choose not to include it. The so-called ‘big blue bump’ seems to disappear in low-luminosity AGNs (Eracleous et al. 2010a). This observation adds further motivation not to include the featureless continuum in the fits.

We admit that there is room for improvements in our spectral fitting. First, we do not use any priors in the fitting. We may obtain better fits if we use priors on correlations between parameters (e.g., one can assume a broad correlation between dust, SFRs, and stellar mass), although it is not very straightforward

to set priors at high redshifts, where we actually would like to apply the method in the future. Also, one can model more realistic star formation histories by including a secondary burst. Despite the simplicity, however, our models deliver good estimates of SFRs and emission line luminosities as shown below.

### 2.3. Accuracy of SFRs and extinction from the spectral fits and the predicted $L_{SF}$

Using the SFRs and dust extinction measurements derived from the model fits, we can now estimate  $L_{SF}$ . But, first of all, we shall quantify how accurate our estimate of SFRs and  $\tau_V$  from the model fits are. In Fig. 1, we compare SFRs from the spectral fits and those from  $H\alpha$  corrected for extinction using the balmer decrement. For the purpose of quantifying the accuracy of  $L_{SF}$ , we remove AGNs using the BPT diagram with the Kauffmann et al. (2003) threshold from the figure for now. We use galaxies with all the  $H\beta$ , [OIII],  $H\alpha$  and [NII] lines detected at  $> 3\sigma$  here.

We obtain reasonably good estimates of SFRs from the spectral fits, although there is a tilt there. We apply a biweight fit and find a log-linear slope of 0.63 and the scatter around the solid line to be only 0.23 dex (a factor of 1.7). As discussed in the appendix, the tilt and the mean offset becomes slightly larger if we use the original  $\tau \propto \lambda^{-0.7}$  law of Charlot & Fall (2000). Note as well that we obtain a better correlation with a log-linear slope of 0.8 if we do not correct for the dust using the Balmer decrement. We will extensively use SFRs from the spectral fits, and we could empirically correct for the observed tilt to obtain more precise SFRs. But, we choose not to do so because it does not change our conclusions in the paper. We try not to use empirical calibrations of the outputs from the spectral fitting throughout the paper as long as they do not affect our main conclusions.

While we can estimate SFRs reasonably well, our dust estimates are not as good as we hoped for. The two component dust model of Charlot & Fall (2000) does not seem to work very well and our dust measurements are almost always smaller than those from the Balmer decrements particularly at low  $\tau_V$ . The median difference between the two extinction estimates is  $\tau_{v, specfit} - \tau_{v, H\alpha/H\beta} = -0.98$ .

From SFR and  $\tau_V$ , we can work out  $L_{SF}$ . In case of  $H\alpha$ , we use the following equation to derive it:

$$L_{H\alpha, SF} = SFR / (7.9 \times 10^{-42} / 1.7) \times \exp(-0.75\tau_V) \quad (2)$$

The conversion factor from SFR to  $H\alpha$  flux is from Kennicutt (1998) and the factor of 1.7 is applied to change the initial mass function from Salpeter (which is assumed in Kennicutt 1998) to Chabrier (Asari et al. 2007). Extinction at the wavelength of  $H\alpha$  is  $0.75\tau_V$ . Fig. 2 compares the predicted  $H\alpha$  luminosity from the spectral fits with the measured luminosity. The figure shows that we can make a fairly accurate (a dispersion of 0.16 dex or a factor of 1.4) prediction of  $H\alpha$  luminosity from the continuum fit. This good correlation might appear surprising given the poor dust estimates, but it is due to the degeneracies between SFR and dust — slightly underestimated SFRs and underestimated dust extinction nearly cancel out and give us good emission line luminosity estimates. We perform a bi-weight fit to the data and obtain a log-linear slope of 0.80. This is a relatively small tilt and and the accuracy of the predicted

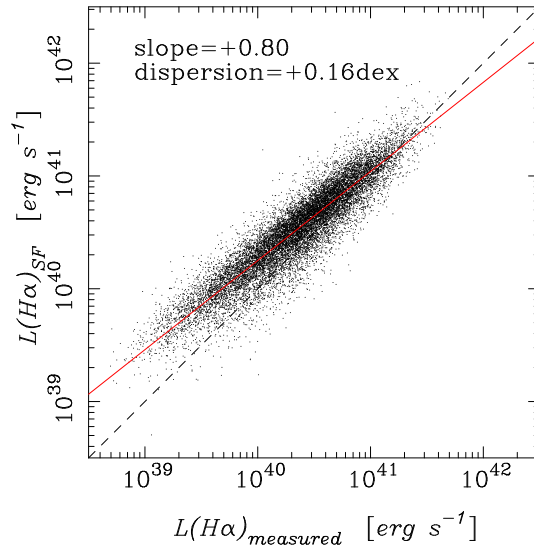
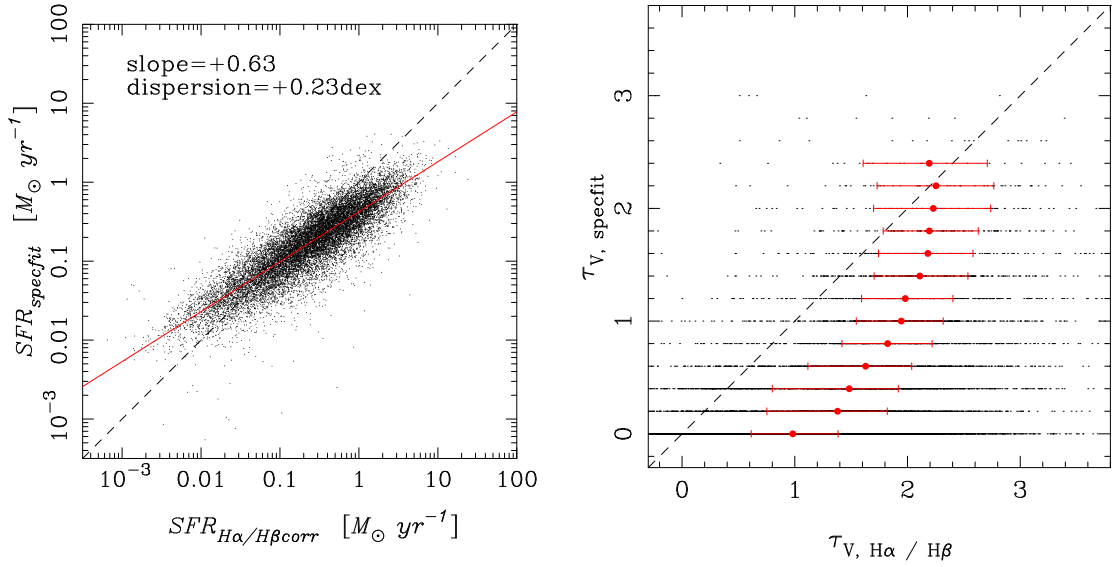


Fig. 2. Predicted  $H\alpha$  luminosity from the spectral fits plotted against measured  $H\alpha$  luminosity. The slope of the log-linear fit and dispersion around it are shown in the plot.

luminosity is encouraging.

We emphasize that Fig. 2 includes all the effects from observations and model fits. As discussed above, our models may not be the most realistic models and there is room to improve the fitting procedure, but we can still make a fairly good prediction of  $L_{SF}$ . Continuum may provide SFRs on different time scales from those from  $H\alpha$ .  $H\alpha$  comes from star forming regions and is a good probe of instantaneous SFRs, while continuum may provide SFRs smoothed over an extended period. The scatter we observe in Fig. 2 is perhaps partly due to the different time scales probed. But, including all these effects, we obtain a remarkable accuracy with only a small tilt. We find that this scatter does not significantly reduce if we use  $H\alpha$  measured at  $> 10\sigma$  only, suggesting that the scatter is primarily due to scatter in  $L_{H\alpha, SF}$ . The errors in the physical parameters from the spectral fits may not be accurate due to correlations between the adjacent wavelength points and to model degeneracies as mentioned above, but the observed dispersion gives us a good quantitative estimate of an error in  $L_{H\alpha, SF}$ , which is a factor of 1.4 with a small tilt.

In addition to the Balmer lines, we make an extensive use of [OII] and [OIII] lines. But, to derive [OII] and [OIII], we need an empirical calibration because these lines have strong dependence on metallicity, but we cannot estimate metallicity of galaxies from the spectral fits as discussed in the appendix. We fit a relationship between observed flux ratios of [OII] or [OIII] to  $H\alpha$  and stellar mass as shown in Fig. 3. The idea is to use stellar mass as a proxy of metallicity given the tight mass-metallicity relation (Tremonti et al. 2004). Using these empirical calibrations, we can now predict [OII] and [OIII] luminosity due to star formation (i.e.,  $L_{SF}$ ) as we know the stellar mass and  $H\alpha$  luminosity from the spectral fits. We find that the predicted [OII] and [OIII] luminosities are slightly tilted with respect to the observed luminosities (a log-linear slope of  $\sim 0.8$ ). The tilt does not strongly affect our results in this paper and those in Paper-II and for simplicity we assume that the



**Fig. 1. Left:** SFRs from spectral fits plotted against SFRs from  $H\alpha$  corrected for the dust extinction using the balmer decrement assuming the extinction law of Cardelli et al. (1989) and intrinsic  $H\alpha/H\beta$  ratio of 2.86 (Osterbrock & Ferland 2006). We plot every 5 objects for clarity. The solid line shows a log-linear fit to the data and the slope and dispersion around the fit are shown in the plot. Note that AGNs identified with BPT are removed from the plot. **Right:**  $\tau_V$  from the spectral fits plotted against  $\tau_V$  from the balmer decrement. The points and error bars show the median and 25th-75th percentile interval (they are shown only at  $\tau_{V, specfit}$  bins with more than 100 galaxies).

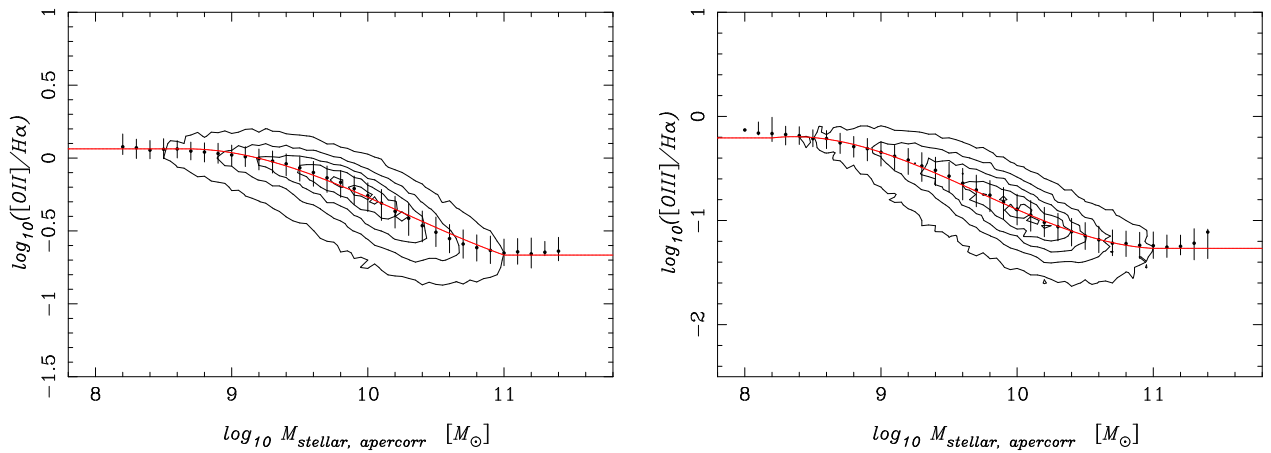


**Fig. 3. Left:** Observed  $[OII]$  to  $H\alpha$  flux ratio plotted against stellar mass. The contours enclose 5%, 25%, 50%, 75% and 95% of the galaxies. The points and error bars show the median and quartile of the distribution in each stellar mass bin. The curve shows the fitted relation. **Right:** Same as the left panel, but  $[OIII]$  to  $H\alpha$  flux ratio is taken in the vertical axis.

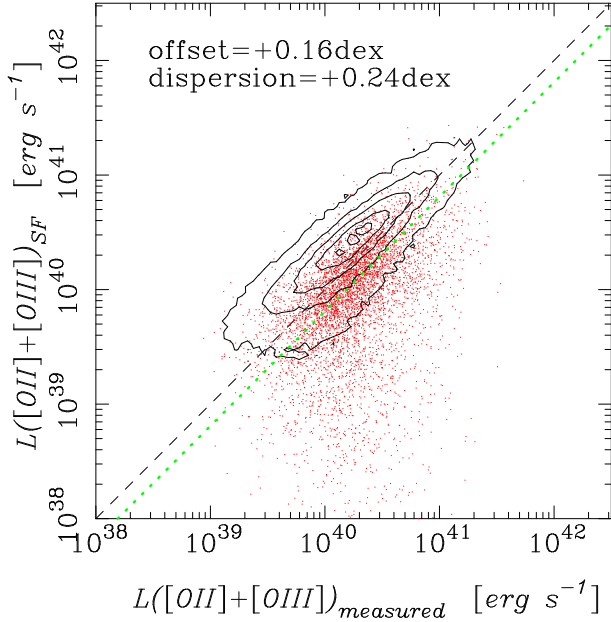


**Fig. 5.** Predicted [OII]+[OIII] luminosities due to star formation plotted against measured luminosities. The contours show star forming galaxies and the dots show AGNs selected from the BPT diagram. Only every 5 AGNs are plotted for clarity. The dotted line shows the threshold of Oxygen-excess and galaxies below it are defined as Oxygen-excess galaxies.

predicted and observed luminosities of all the emission lines are correlated with a log-linear slope of 1 with a small constant offset.

#### 2.4. Line of choice: $H\alpha$ , [OII], or [OIII]?

Now we have developed a technique to predict  $L_{SF}$  for the strong lines such as [OII], [OIII], and  $H\alpha$ . Which line(s) should we use to identify AGNs? We compare these three lines in Fig. 4. We define AGNs using the BPT diagnostics with the Kauffmann et al. (2003) threshold just as a guide line for now and show them with dots in the figures. Interestingly, the collisionally excited Oxygen lines of AGN hosting galaxies show a clear offset with respect to star forming galaxies, while  $H\alpha$  line shows only a small offset. This is what expected from the BPT diagram, which clearly shows enhanced strengths of collisionally excited lines compared to the Balmer lines in AGNs (AGNs form a sequence towards the top-right corner of the BPT diagram, not to the bottom-left corner). In this work, we shall use [OII] and/or [OIII] for our purpose of AGN identification.

As we will show in Paper-II, the ionization state of the narrow line regions in AGNs spans a wide range. Given this wide range of ionization, we deem that a sum of [OII] and [OIII] is likely a better indicator of AGN activities than either one of them because these two lines balance each other in gaseous nebulae and the sum of them is more robust against variations in the ionization states. We therefore use the sum of the two Oxygen lines to identify and to characterize AGNs.

Using the technique developed above, we can predict the [OII]+[OIII] luminosities fairly well as shown in Fig. 5. We define *Oxygen-excess galaxies* as those with

$$\log_{10} \frac{L_{[OII]+[OIII],measured}}{L_{[OII]+[OIII],SF}} - \log_{10} L_{[OII]+[OIII],offset} > 1.5 \times \log_{10} \sigma(L_{[OII]+[OIII],SF}), \quad (3)$$

where  $L_{[OII]+[OIII],offset}$  is a systematic offset between the predicted luminosity and measured luminosity for star forming galaxies (+0.16 dex as shown in Fig. 5) and  $\sigma(L_{[OII]+[OIII],SF})$  is an accuracy of our luminosity predictions (0.24 dex). Our selection criterion is that if an object has an [OII]+[OIII] luminosity that exceeds the expected luminosity due to star formation by  $> 1.5\sigma$ , it is an Oxygen-excess object. This sigma cut is a trade off between completeness and contamination (e.g., if we reduce the threshold to  $1\sigma$ , we have a better sampling of BPT AGNs at the cost of increased contamination of star forming galaxies). Our choice of  $1.5\sigma$  is simply a compromise between them, but we have confirmed that our results do not significantly change if we change it to  $1\sigma$  or  $2\sigma$ . The adopted threshold is shown as the dotted line in Fig. 5. We further require a significant detection of [OII]+[OIII] at  $> 3\sigma$  to ensure that we do not suffer from noises. Since the idea is to identify Oxygen emission line excess, we dub our method ‘‘Oxygen-excess method’’.

As a quick check of the Oxygen-excess method developed here, we plot in Fig. 6 the distribution of the Oxygen-excess galaxies on the BPT diagram. 43% of galaxies in our sample show strong enough emission lines to apply the BPT diagnostics and are plotted as the contours in the figure. Among these strong emission line objects, we find that our SF/AGN classifications agree with BPT for 85% of objects. The Oxygen-excess objects are mostly (75%) in the AGN region of the BPT diagram. The rest of them are in the SF region, but we note that the SF/AGN threshold of Kauffmann et al. (2003) is arbitrary defined. If we use the criterion proposed by Stasińska et al. (2006), the fraction increases to 87%.

The right plot of Fig. 6 shows the distribution of projected distances of the galaxies to the threshold curve. Galaxies distribute contiguously around the (arbitrary set) threshold. This continuous sequence from star forming galaxies to AGNs probably represents a wide range of AGN activities with respect to underlying star formation. The BPT diagnostics misses weak AGNs in actively star forming galaxies (so does our method but with a improved sensitivity to weak AGNs; see the next section and Paper-II) and it would not be surprising at all if some of the galaxies in the star forming region of the diagram actually host AGNs. In fact, the Oxygen-excess objects in the star forming region of the diagram are skewed towards  $distance \sim 0$ , while normal star forming galaxies form a peak around  $distance \sim -0.15$ . If these Oxygen-excess objects were pure contamination, we would have seen a peak at  $distance \sim -0.15$  with an extended tail to  $distance \sim -0.5$ . The skewed distribution of the Oxygen-excess objects suggests that they are not pure contamination of star forming galaxies. We will make further attempts to characterize our method in the next section.

In addition to the most commonly used BPT diagnostics, we also present [OIII]/ $H\beta$  vs. [OI]/ $H\alpha$  and [OIII]/ $H\beta$  vs. [SII]/ $H\alpha$  diagrams (Veilleux & Osterbrock 1987) in the Appendix for completeness. As pointed out by earlier papers (e.g., Kewley

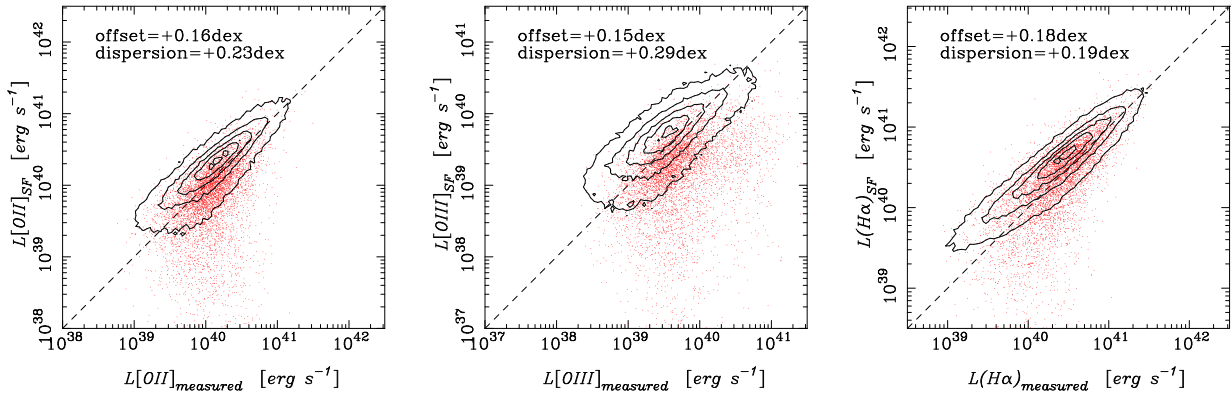


**Fig. 4.** Predicted line luminosities due to star formation plotted against measured line luminosities. The panels show, [OII], [OIII], and H $\alpha$  from left to right. We show objects with significant line detections ( $> 3\sigma$ ). In each panel, the contours show star forming galaxies and the dots show AGNs selected from the BPT diagram (plotted every five objects). The dashed lines show  $L_{SF} = L_{measured}$ . An offset from the dashed line and dispersion in  $\log(L_{SF}/L_{measured})$  in each panel are for star forming galaxies.

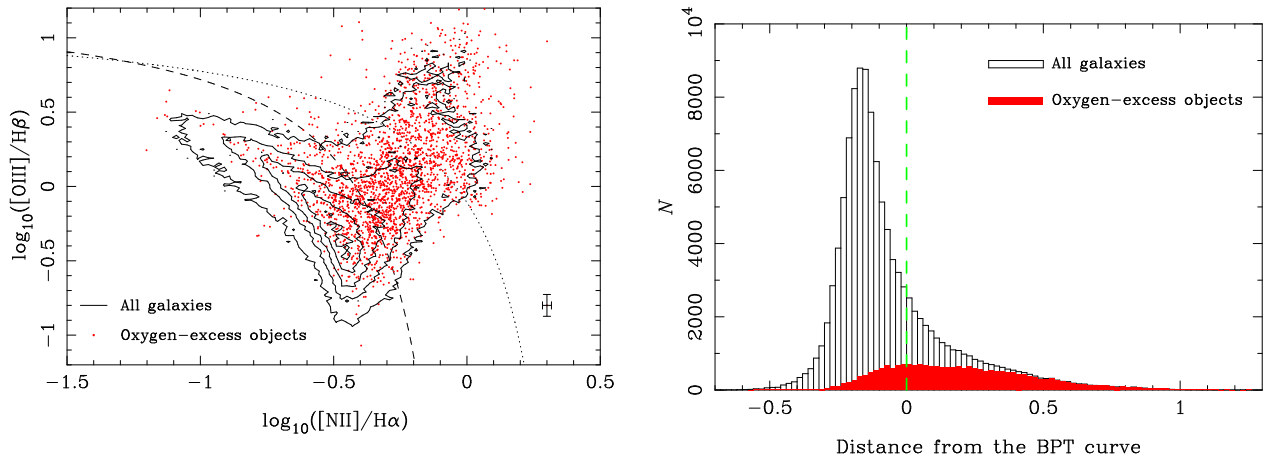


**Fig. 6.** **Left:** BPT diagram. The contours encircle 5%, 25%, 50%, 75% and 95% of all the galaxies used here (i.e.,  $0.02 < z < 0.1$  and all the four lines detected at  $> 3\sigma$ ). The dots show Oxygen-excess objects (plotted every five objects). The dashed curves is from Kauffmann et al. (2003). Just for a reference, we also show the Kewley et al. (2001) threshold as the dotted curve. The cross on the bottom-right shows the median error in the line ratios. **Right:** The distribution of 'distance' of galaxies from the Kauffmann et al. (2003) curve in the left panel. The negative distance means that galaxies are in the star forming region, while the positive distance means that galaxies are in the AGN region. The vertical dashed line is the Kauffmann et al. (2003) threshold. The open and filled histograms show all the galaxies and Oxygen-excess galaxies.

et al. 2006; Stasińska et al. 2006), the separation between star formation and AGN sequences is less clear if we use [OI] or [SII] in place of [NII]. [NII] seems to work better because the [NII]/H $\alpha$  ratio saturates at high metallicities (Kewley & Dopita 2002) due likely to its secondary nature (Kewley & Dopita 2002; Stasińska et al. 2006). But, the [OI] and [SII] lines are interesting in their own right. For instance, the [OI] line comes from partially ionized nebulae and hence it is sensitive to the hardness of ionizing spectrum and is a good probe of AGNs. Readers are referred to Appendix for further discussions.

Finally, we shall emphasize that the Oxygen-excess method can be applied at much higher redshifts compared to BPT. Although [OII]+[OIII] is the most effective set of lines, one can in principle use any line to identify an emission line excess. A practical application of the method would be to use [OII] only. One has to take a risk of missing high ionization AGNs that exhibit weak [OII], but the gain is that one can go up to  $z \sim 1.7$  with red-sensitive optical spectrograph to study the AGN evo-

lution over a wide redshift range. Our method will be an ideal method to identify AGNs and study their host galaxy properties in on-going/near-future massive spectroscopic surveys such as SDSS-III Baryon Oscillation Spectroscopic Survey.

### 3. Comparisons between Oxygen-excess, BPT, X-ray and radio sources

Following the development of the Oxygen-excess method, we make extensive tests of the method by comparing with other AGN detection methods in this section. First, we further compare with the BPT diagnostics. A significant fraction of galaxies in our sample (43%) show too weak emission lines to apply the BPT diagnostics, but they have strong enough Oxygen lines to apply the Oxygen-excess method. We test how well our method works in such weak emission line galaxies by stacking spectra. The stacked spectra are also useful to characterize average properties of various classes of objects. We then compare

with X-ray sources identified in archival Chandra observations and also with radio sources from FIRST.

Before we present our results, it is important to emphasize that none of the Oxygen-excess, BPT, X-ray, and radio methods is a perfect method to identify AGNs. Each method has pros and cons and they all suffer from incompleteness and contamination. The most relevant numbers to quote in this section would be fractions of missing AGNs and contaminating non-AGNs in the Oxygen-excess objects. But, we are unable to provide these numbers because no AGN identification method gives a complete sampling of AGNs. Nonetheless, we make an attempt to quantify whether a majority of the Oxygen-excess are real AGNs or not. Note that we cannot reach any clear conclusion in intermediate types of objects that are fundamentally difficult to classify (see Ho 2008 for a review of the subject). Also, we will discuss objects that are photo-ionized by non-AGN sources in section 3.4.

### 3.1. Stacked objects on the BPT diagram

We define classes of galaxy populations in Table 1 to compare the Oxygen-excess objects with the BPT objects. The notation is defined as 'O' and 'B' stand for Oxygen-excess and BPT. '+' and '-' mean AGN and SF. For example, O+B- are the objects that are identified as AGN by the Oxygen-excess method, but are classified as SF by BPT. We use an 'n' for objects we cannot apply the Oxygen-excess or BPT method due to weak emissions. Note that we use the threshold by Kauffmann et al. (2003) to define AGN and SF on the BPT diagram.

In our spectral fitting described in the last section, we subtract the continuum using the best-fitting model template and further by applying the median filter to remove the residuals. We stack these continuum subtracted spectra in each class using the inverse-variance weights to make the average emission line spectra. We also perform the median stacking in addition to the inverse-variance stacking. The emission line strengths in the stacked spectra are somewhat different between these two stacking techniques, but the line ratios, which we will soon discuss, are not very different. Note that we combine the spectra in apparent flux density, not in distance corrected luminosity density (i.e., only the wavelengths are corrected to rest-frame) because the AGN/SF classification is limited by the observational flux limit (this is especially relevant to O+Bn, O-Bn, and OnBn classes) and we would like to show typical observed flux densities of objects in these classes and compare them with stronger emission line objects. We have confirmed that the line ratios we discuss below are essentially the same regardless of whether we correct for the distance or not.

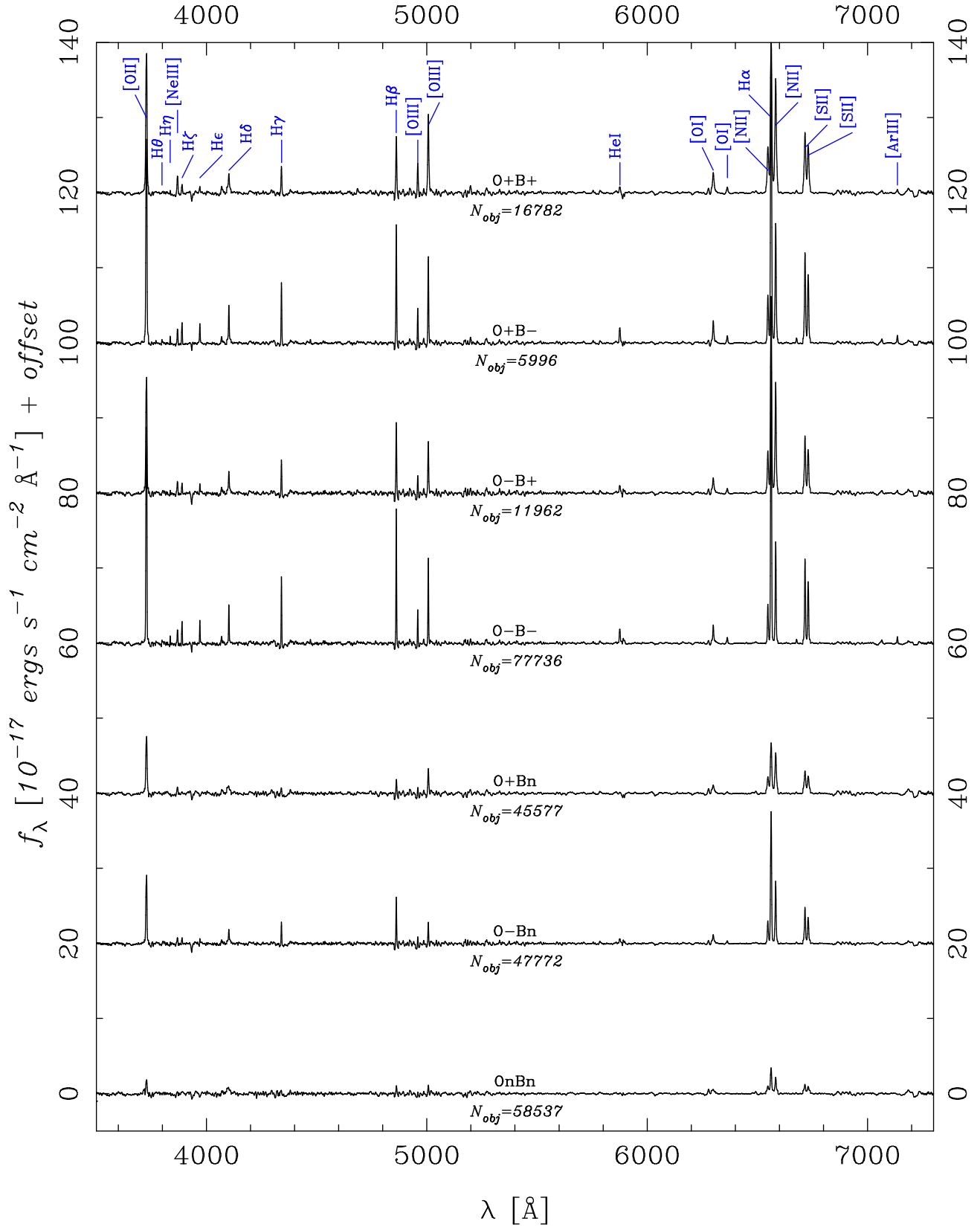
Fig. 7 presents the stacked spectra of all classes. Note the very high quality of the stacked spectra. A typical emission line fluxes in the OnBn class is comparable to the typical noise level of the SDSS spectra. The stacked spectra are of sufficient signal-to-noise to measure emission line fluxes for all class of objects. We can now measure the line ratios and study their average properties. O+Bn and O-Bn will be particularly interesting because we cannot apply the BPT diagnostics to these galaxies individually. We show locations of the stacked objects on the BPT diagram in Fig. 8 and discuss each class of objects below. The numbers in the parenthesis are the fractions of objects in that class to the entire sample.

- **O+B+ (6.3%):** We observe strong emission lines in the stacked spectra. The line flux ratios on the BPT diagram indicate that the galaxies host AGNs.
- **O+B- (2.3%):** This is an interesting class of objects. The galaxies are classified as star forming galaxies on the BPT diagram, but we observe an Oxygen flux excess. The stacked spectrum ranges from the middle of the star forming sequence to the threshold line of Kauffmann et al. (2003). The observed offset to the threshold compared to B-O-, which are nearly pure star forming galaxies (see below), suggests that these galaxies may harbor weak AGNs with underlying active star formation. But, the BPT diagram does not give us an estimate of AGNs and contaminating star forming galaxies. This is one of the difficult classes to characterize.
- **O-B+ (4.5%):** The galaxies are defined as AGNs from the BPT diagram, but we do not observe a significant Oxygen flux excess. The stacked spectra and the location on the BPT diagram show that these galaxies likely host AGNs with active underlying star formation. The X-ray analysis below also suggests that they are likely AGNs. The majority of the galaxies in this class are AGNs and our method misses them. It could be that we miss them due to statistical fluctuations of our flux predictions (the scatter is a factor of 1.7; Fig. 5). But, it could also be that AGN continuum gives a non-negligible contribution to the overall continuum spectra. AGN continuum is likely a power-law form in the optical wavelengths, making the spectra bluer. Although such AGN continuum is typically fairly weak in weak AGNs (Schmitt et al. 1999), we may over-estimate SFRs if AGN continuum is happen to be strong. As a result, we may miss AGNs. As mentioned earlier, we cannot measure the amount of such continuum contribution with our spectral fits well. GALEX photometry may give us an insight into AGN continuum, but our poor estimates of dust extinction would not allow us to study near-far UV luminosities because of the strong sensitivity to dust. A more sophisticated spectral fitting would be needed. We characterize the host galaxy properties of O-B+ in the Appendix and show that this missing AGN population does not affect our conclusions in Paper-II.
- **O-B- (29.4%):** These objects are in the star forming region on the BPT diagram and we do not observe an Oxygen flux excess. The stacked spectrum is indeed in the middle of the star forming region of the BPT diagram. Therefore, these objects are likely star forming galaxies.

We can apply the BPT diagnostics to all the objects discussed so far<sup>1</sup>. We shall emphasize that the SF/AGN classification by the Oxygen-excess method is consistent with BPT for 85% of the objects (O+B+ and O-B-). Intermediate cases (O+B- and O-B+) are somewhat challenging to fully characterize, but they make up only 15% of the strong emission line objects. We also emphasize that we could apply the BPT di-

<sup>1</sup> If we use the Kewley et al. (2001) threshold to define AGN/SF, the fractions in the above classes are 2.5%, 5.8%, 0.3%, 32.5% for O+B+, O+B-, O-B+, and O-B-, respectively.

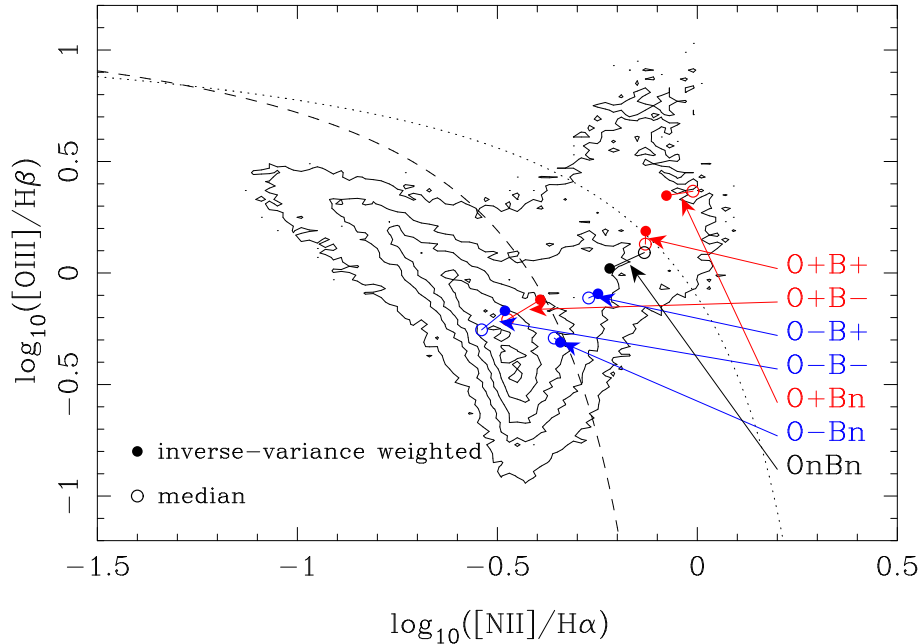




**Fig. 7.** Stacked spectra. From top to bottom, the spectra are for O+B+, O+B-, O-B+, O-B-, O+Bn, O-Bn, and OnBn, respectively. Most prominent emission lines are labeled. The numbers of objects used for the stacking are shown as well.

**Table 1.** Galaxy population classes.

	BPT-AGN	BPT-SF	4 lines unavailable
Oxygen excess	$O + B+$	$O + B-$	$O + Bn$
No Oxygen excess	$O - B+$	$O - B-$	$O - Bn$
Oxygen unavailable	—	—	$OnBn$

**Fig. 8.** BPT diagram. The contours show galaxies with strong emission lines as in Fig. 6. The locations of the stacked objects are indicated by the circles and arrows. The filled and open circles are measured from the inverse-variance weighted stacking and from the median stacking, respectively.

agnostics only to 43% of objects in our sample. Although we define our sample at  $0.02 < z < 0.10$ , which is below the median redshift of the Main galaxy sample ( $z \sim 0.1$ ), more than a half of the objects remain unclassified. This is where our method has a great advantage — our method can be applied to nearly twice as many objects as BPT. We discuss these weak emission line objects below.

- **O+Bn (17.2%):** The galaxies in this class do not show strong enough lines to apply the BPT diagnostics, but their  $[OII]+[OIII]$  lines are strong enough to apply our method. A large fraction of galaxies in the O+Bn and O-Bn classes demonstrates the sensitivity of our method to low-luminosity objects. The emission lines in the stacked spectrum are weak as expected.  $H\beta$  is often the weakest line among the four lines used in the BPT, and that limits the sensitivity of BPT to low-luminosity AGNs. The line ratios from the stacked spectra clearly show that these objects actually host AGNs. This is a strong proof that the Oxygen-excess method works well in identifying such low-luminosity AGNs. The X-ray and radio analyses presented below also shows that most of the objects are likely AGNs. We shall note that there has been a considerable debate as to whether low-luminosity, low-ionization objects (LINERs; Heckman 1980) are powered by AGNs. There are other energy

sources proposed in the literature that can produce weak LINER-like emission. We discuss those fake AGNs in Section 3.4.

- **O-Bn (18.1%):** The stacked spectrum shows weak emission lines.  $H\beta$  is stronger than  $[OIII]$  and this class of objects unlikely host strong AGNs. The stacked object lies on the border of the threshold line in the BPT diagram. This suggests that, while the majority of the objects do not host AGNs, we may have small contamination of AGNs (see the radio analysis below). O+Bn and O-Bn are the classes for which we can apply the Oxygen-excess method only. The positions of these objects on the BPT diagram clearly demonstrate that our classification for such weak emission line objects is fairly reasonable.
- **OnBn (22.1%):** A large fraction of all the objects do not show even weak emission lines and fall in this category. If we stack their spectra, very weak emission lines emerge. Most of the lines are comparable strength to typical noise level in the SDSS spectra. The line ratios in Fig. 8 indicate that LINERs reside in such apparently quiescent galaxies. We also observe that a fraction of them is detected in radio despite their weak emission (see below).

To sum up, for bright objects for which we can apply the BPT diagnostics, the Oxygen-excess method gives the consistent SF/AGN classifications for 85% of the objects. While

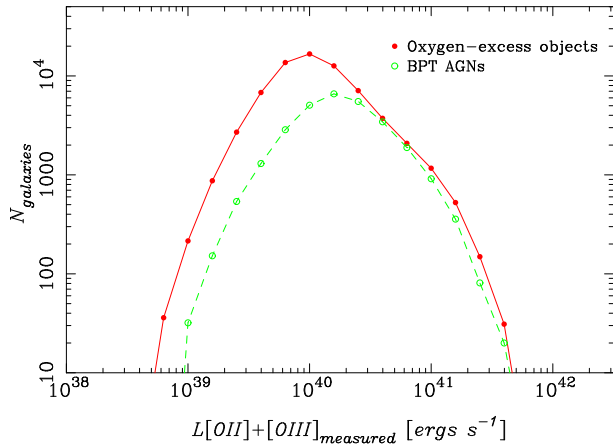


**Fig. 9.**  $L_{[OII]+[OIII]}$  distributions of the Oxygen-excess objects (filled circle) and BPT AGNs (open circles).

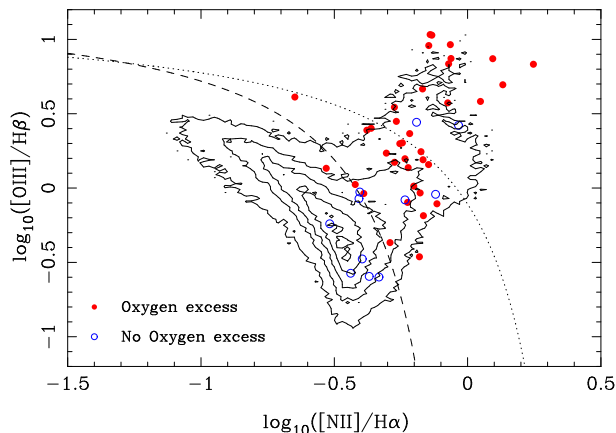


**Fig. 10.** Distribution of X-ray sources on the BPT diagram. The curves and the contours are as in Fig. 6. The filled and open points show X-ray sources with and without Oxygen flux excess, respectively.

the BPT diagnostics is applicable to 43% of all the objects, the Oxygen-excess method is applicable to 78%. This results in a higher fraction of the Oxygen-excess objects (26%) than BPT AGNs (11%). Fig. 9 illustrates our sensitivity to low-luminosity objects. The Oxygen-excess method can identify a significant number of low-luminosity objects that are missed by BPT. The stacked spectra show the average properties of objects in each class. Except for a small fraction of the discrepant cases (O+B- and O-B+, 7% of total), the stacked spectra on the BPT diagram show that the AGN/SF classifications are made well. In particular, low-luminosity objects for which the BPT is not applicable are classified fairly well. This is an encouraging result and motivates us to perform a further test of the method using X-ray and radio data.

### 3.2. X-ray sources

We base our X-ray analysis on the CSC-SDSS cross-match catalog release 1.1 from the Chandra website<sup>2</sup> (Evans et al. 2010). The catalog has Chandra sources from archival data

<sup>2</sup> <http://cxc.harvard.edu/csc/>

matched to SDSS objects. Due to the nature of its serendipity, the data depth varies across the sky and the data are not defined in any systematic way. However, the serendipity in turn allows us to perform a statistical test of our method because any specific types of Oxygen-excess objects do not prefer any particular patch of Chandra observations.

We use SDSS objects that have point-like Chandra counterparts within 2 arcsec from the center to ensure that we are looking at sources at the galaxy centers, while accommodating the PSF degradation at large angle from the focal axis. This results in 56 X-ray sources, which are the subject of the analyses in this subsection. We have also cross-matched the archival XMM-Newton sources (Watson et al. 2009). We find that the conclusions in this section remain the same if we use the XMM sources, but there seems a slightly increased amount of non-AGNs sources possibly due to the poorer angular resolution of XMM compared to Chandra<sup>3</sup>. We thus use the Chandra data for the analysis here.

We do not correct for absorption due to the Galactic neutral hydrogen because essentially all the objects have a low hydrogen column density due to the Galaxy of a few times  $10^{20} \text{cm}^{-2}$  (Dickey & Lockman 1990). Based on Morrison & McCammon (1983), we estimate that the absorption in the hard band (2-7keV) is negligible. The absorption is still small in the soft band (0.5-1.2keV) with an optical depth of a few times  $10^{-1}$ . The correction for intrinsic absorption requires sufficient X-ray photons and a detailed spectral analysis, which is beyond the scope of this work. However, an intrinsic absorption is likely below  $10^{22} \text{cm}^{-2}$  at the X-ray luminosity range we explore here (Mainieri et al. 2007). At this column density, a hard X-ray luminosity is largely unaffected by absorption. Our hard X-ray luminosity should therefore be reasonable estimates.

First, we put the X-ray objects in the BPT diagram in Fig. 10. Note that we cannot show X-ray detected O+Bn, O-Bn, and OnBn objects in the diagram due to their weak emission. Most of the X-ray sources are in the AGN region of the diagram. There are several sources in the star forming region, but most of them do not show any Oxygen excess.

Due to the serendipitous nature of the X-ray catalog, we can compare the relative frequency of X-ray detections of various classes of objects defined in Table 1. We normalize the X-ray detection frequency of the B+O+ objects to unity and show the relative frequencies in Table 2. We also show the X-ray properties of the objects in Fig. 11. There are several energy sources of X-ray emission: AGNs, supernova remnants, high/low-mass X-ray binaries, and hot thermal plasma in the halos. To quantify the dominance of AGNs in each panel, we define a region of the diagram where we expect contamination of non-AGN sources as the dashed line. This definition is motivated by the fact that these non-AGN sources are likely soft, low-luminosity sources. For example, Irwin et al. (2003)

<sup>3</sup> We have cross-matched 108 objects with the archival XMM sources within  $1\sigma$  positional error (but we impose a maximum separation of 3 arcsec). We find that a larger fraction of objects have soft X-ray emission, whose origin could both be AGN and non-AGN sources, compared to the Chandra sources. Although we restrict the sources to be consistent with PSF sizes, the galaxies optically extend on a comparable angular size to the resolution of XMM. We suspect that the XMM luminosities suffer from increased contamination from non-AGN sources such as X-ray binaries than Chandra.

**Table 2.** X-ray and radio detection rates in each class normalized to that of B+O+. Objects that could be contaminated by non-AGN X-ray/radio emission are excluded from the statistics (see text for details). Due to this conservative analysis, the numbers here should not be regarded as purity of the AGN sample. The numbers also suffer from X-ray/radio sensitivity limits and the fractions are naturally lower in lower luminosity AGNs.

	X-ray	Radio
$O + B+$	$1.000 \pm 0.186$	$1.000 \pm 0.035$
$O + B-$	$0.097 \pm 0.097$	$0.240 \pm 0.028$
$O - B+$	$0.242 \pm 0.108$	$0.088 \pm 0.012$
$O - B-$	$0.015 \pm 0.011$	$0.009 \pm 0.001$
$O + Bn$	$0.140 \pm 0.042$	$0.258 \pm 0.010$
$O - Bn$	$0.012 \pm 0.012$	$0.027 \pm 0.003$
$OnBn$	$0.040 \pm 0.020$	$0.083 \pm 0.005$

showed that most of the low-mass X-ray binaries have a hardness ratio less than 0 between the soft (0.3–1.0keV) and hard (2–6keV) bands. The definition is further motivated to include most of the O-B- galaxies whose X-rays are likely star formation or other non-AGN origins. But, this is still a somewhat arbitrary definition and should not be over-interpreted. AGNs may well populate in the dashed box. Note that we have excluded these possible non-AGNs from the statistics in Table 2 to be conservative.

We discuss each class of objects in what follows.

- **O+B+** : Most of the objects ( $\sim 80\%$ ) show  $L_X > 10^{41} \text{ erg s}^{-1}$  with relatively hard spectra. They are likely AGNs.
- **O+B-** : We have only one X-ray source, which is likely an AGN due to its high luminosity ( $L_X \sim 10^{42} \text{ erg s}^{-1}$ ). We do not further discuss this class of objects due to the poor statistics.
- **O-B+** : Many of the objects in this class are relatively luminous X-ray sources with medium hardness. They are likely AGNs. Our method misses this class of objects.
- **O-B-** : These objects are likely star forming galaxies. Most of them have soft, low X-ray luminosity. But, there are luminous, medium hardness sources, which are likely AGNs. The X-ray detection rate is only 2% of that of O+B+ and such AGNs are very rare.
- **O+Bn** : These are AGN candidates identified by the Oxygen-excess method, but their emission lines are too weak to apply the BPT diagnostics. The distribution of objects in Fig. 11 is relatively similar to that of B+O+, and most objects in this class are likely AGNs. The X-ray detection rate is not as high as O+B+, but it is probably because AGNs in this class are weaker given the weak emission lines. X-rays clearly show that the Oxygen-excess method works well in identifying such weak AGNs.
- **O-Bn** : We do not observe any significant Oxygen flux excess in those objects, and most of the X-ray sources in this class are indeed low-luminosity soft sources with an exception of a very hard source. As inferred from the stacked spectrum, a small fraction of objects in this class may be real AGNs. But, we note a very small X-ray

detection rate in Table 2 (1%).

- **OnBn** : X-ray detections of these objects may be surprising as we do not observe any significant emission lines. There seems a sequence of soft X-ray objects with X-ray luminosities between  $\sim 10^{39}$  and  $\sim 10^{40} \text{ erg s}^{-1}$ . We find a clear correlation between the X-ray luminosities of these objects and their stellar mass, which lends support to the low-mass X-ray binary origin (Kim & Fabbiano 2004). It may also be that diffuse thermal emission contributes to the observed X-ray luminosity (Flohic et al. 2006). There are a few sources with hardness ratio around 0. We exclude the possibility of the supernova and high-mass X-ray binary origin for these sources because the host galaxies are quiescent galaxies with very little on-going star formation. Although we cannot be conclusive, their hardness ratios seem to suggest that they are unlikely due to low-mass X-ray binaries. They may possibly be obscured AGNs with very weak optical emission lines.

The comparisons with X-ray sources give another quantitative estimate of the robustness of the Oxygen-excess method. Although X-rays suffer from contamination from non-AGN sources, the numbers from conservative analyses in Table 2 and Fig. 11 suggest that the Oxygen-excess method separates AGNs from star forming galaxies well, although it does miss a fraction of AGNs (e.g., O-B+). The SF/AGN classifications of low-luminosity objects for which BPT is not applicable (i.e., O+Bn and O-B-) are good (Fig. 11), demonstrating its sensitivity to low-luminosity AGNs.

### 3.3. FIRST sources

We turn our attention to radio sources. Radio wavelengths have also been used to identify (distant) AGNs (Miley & De Breuck 2008 and references therein). In this subsection, we use data from the FIRST survey (Becker et al. 1995; White et al. 1997) to study the properties of the Oxygen-excess objects.

The SDSS objects and FIRST sources are cross-matched within 1 arcsec. We have confirmed that our results are not sensitive to the matching radius (a matching radius of 2 arcsec gives the same results). This is simple positional matching and we may well miss extended radio sources such as jet lobes. However, such extended radio emissions are relatively rare ( $\sim 10\%$ ; Lin et al. 2010) and they should not strongly alter our conclusions. We do not reject extended sources from the matching because AGN point sources may be buried under extended radio emission due to star formation due to the poor spatial resolution of FIRST. In total, we have 1,747 matches in our sample. We adopt  $f_{integrated}$  from the FIRST catalog as radio power. Note that our results remain essentially the same if we use  $f_{peak}$ . We apply the  $k$ -correction to the radio power assuming a power-law spectrum of  $f_\nu \propto \nu^{-0.8}$  (Condon 1992).

We plot in Fig. 12 the distribution of radio detected sources on the BPT diagram. The radio detected objects tend to spread around the AGN sequence and extend to the bottom of the SF sequence. This is in contrast to X-ray sources, which are mostly located away from the Kauffmann et al. (2003) threshold curve as shown in Fig. 10. This is partly due to increased contamination from star formation activities in radio wave-

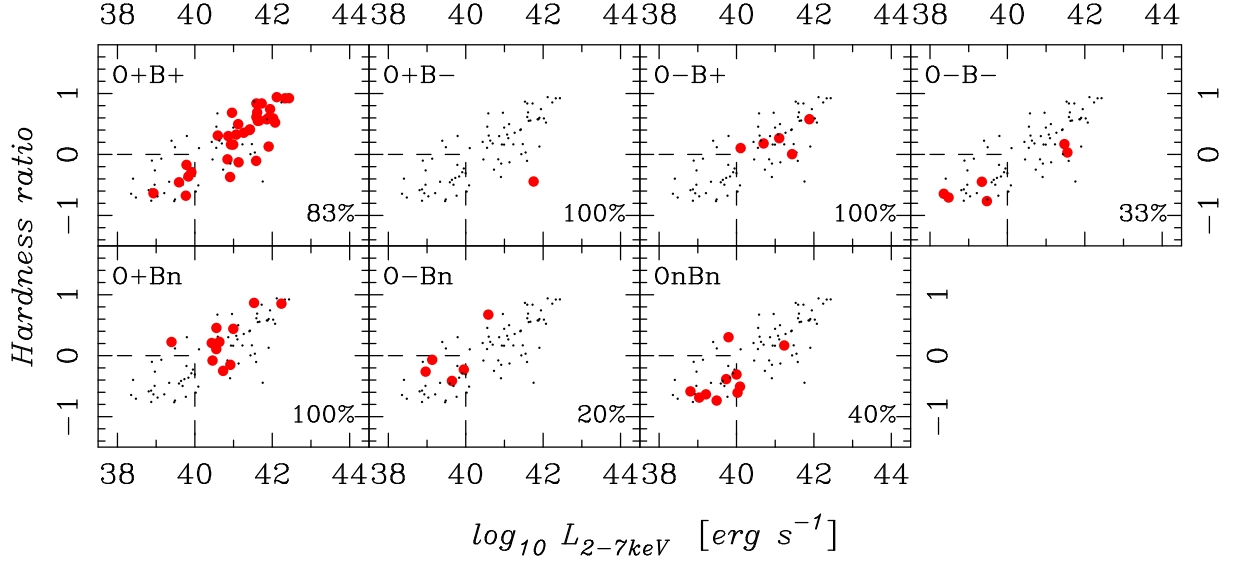


**Fig. 11.** Hardness ratio between soft (0.5 – 1.2 keV) and hard (2.0 – 7.0 keV) bands plotted against hard X-ray luminosity. The panels show subclasses of AGNs defined in Table 1. The dots are all the sources and the points are those in each class. The dashed rectangle on the bottom-left of each panel defines the region, in which we expect contamination of star forming galaxies or other non-AGN sources. The numbers in each panel shows the fraction of objects outside of the rectangle.

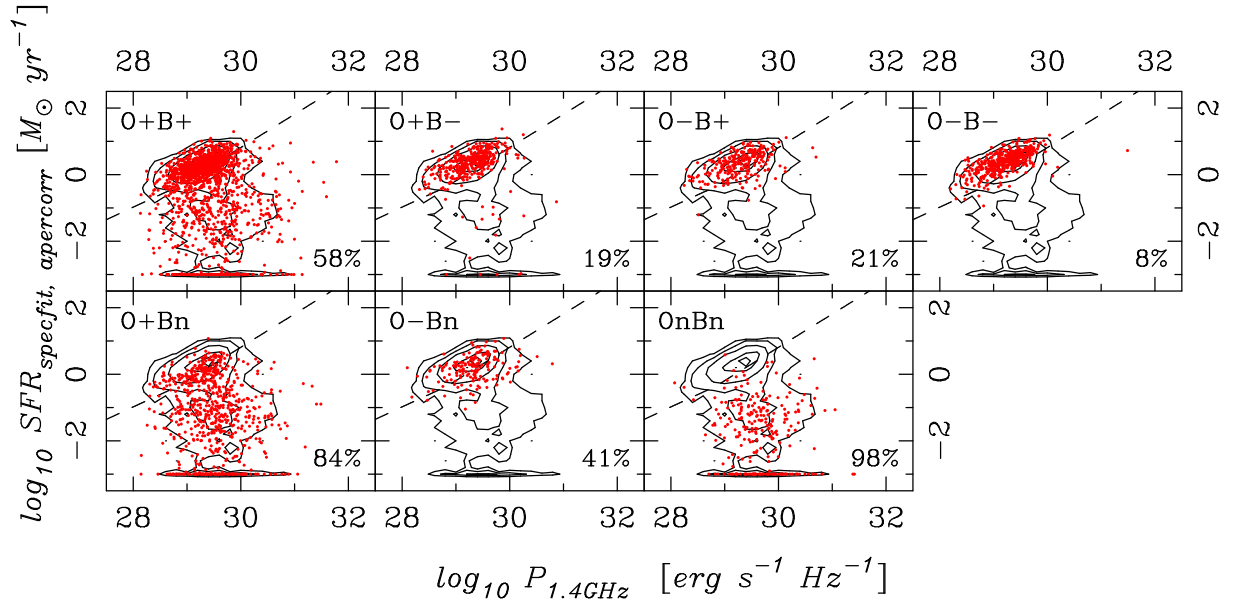


**Fig. 13.** SFRs against radio power. The panels show each class of AGNs defined in Table 1. The contours are all the radio sources and the dots are those in each class. The dashed curve is the SFR-radio power relation from Hopkins et al. (2003) shifted downwards by 0.7 dex (i.e., a factor of 5). Objects below the curve are likely dominated by AGNs and the numbers in each panel shows the fraction of objects below the curve.

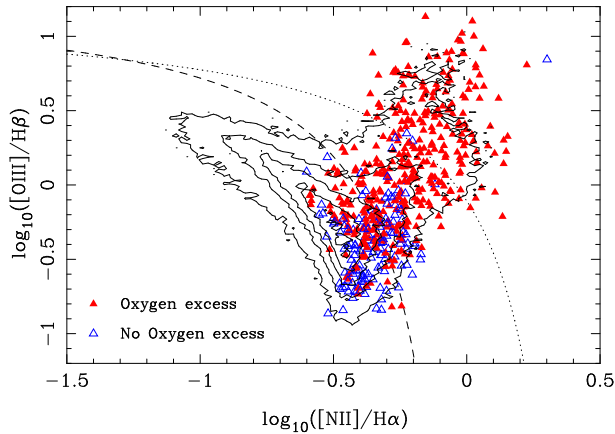


**Fig. 12.** As in Fig. 10, but here we plot objects detected in the FIRST survey.

lengths than in X-rays.

Fig. 13 shows SFRs from the spectral fits against the radio power for each class of objects defined in Table 1. A star formation sequence of galaxies can be seen at the top-left corner of the diagram. We shift the radio power – SFR relation from Hopkins et al. (2003) downwards by a factor of 5 to separate AGN-dominated and SF-dominated objects as shown by the dashed curve. A large fraction of O+B+ objects are dominated by star formation, which is in contrast to X-rays (Fig. 11). This illustrates the elevated contamination from star formation in radio wavelengths. But, we emphasize that not all the galaxies in the star forming region of the diagram are pure star forming galaxies and they may well host AGNs, whose radio emission due to AGN is weaker than that due to star formation. We remove such galaxies from the analysis just to be conservative.

Despite the significant contamination from star formation, the FIRST detection rates shown in Table 2 are fairly useful. As expected, O+B+ and O-B- show the highest and lowest radio detection rates, respectively. Interestingly, O+B- shows a relatively high detection rate. This is encouraging because it shows that not all the objects in this class are contamination and some of the O+B- objects are real AGNs. We comment on the other classes below.

- **O+Bn** : As expected from their weak emission lines, galaxies in this class do not show strong on-going star formation. Most of the objects are not in the star forming region of the diagram and they are likely AGNs. We note that those in the star forming region occupy only the bottom half of the star forming sequence (compare with O-B-, for example), suggesting that even these galaxies have some level of AGN activities. We have shown from the stacking and X-ray analyses that this class of objects are mostly real AGNs. This radio analysis adds even further support to it.
- **O-Bn** : Roughly 40% of the radio detected sources are likely AGNs. If we compare the panels for O+Bn and O-Bn, the classifications look reasonable, but it seems that we do misclassify a fraction of AGNs in this class as already suggested in the stacking analysis. However, the radio detection rate in Table 2 is fairly low and we do

not regard this as a big issue.

- **OnBn** : Some of the apparently quiescent galaxies host AGNs. The radio detection rate is 8% of O+B+, which may be relatively high for such quiescent galaxies. This class of objects clearly shows that we cannot identify all AGNs with optical methods only. Deep multi-wavelength data are essential to sample the entire AGN populations.

The radio detections provide another interesting test of the Oxygen-excess method. While we do suffer from a level of contamination and incompleteness, the Oxygen-excess method overall works well. In fact, the radio detection rates in Table 2 are the highest where we observe excess Oxygen luminosities.

To summarize, we have compared the Oxygen-excess method with BPT, X-ray and radio. As mentioned at the beginning of this section, it is hard to quantify the purity and incompleteness of the Oxygen-excess method because no AGN identification method gives a complete sampling of AGNs. But, the stacked spectra show that the SF/AGN classifications are on average very reasonable and the X-ray and radio analyses give a support to it. The results from these analyses all lead us to conclude that the Oxygen-excess method is a good statistical tool to identify AGNs. In particular, it is fairly sensitive to low-luminosity AGNs for which BPT is not applicable. It of course suffers from incompleteness (e.g., O-B+) and contamination (e.g., a fraction of O+B- galaxies) as all the other methods do, but it classifies AGNs and star forming galaxies well. It is a powerful statistical tool to identify AGNs from spectroscopic data.

### 3.4. Ionizing source — accreting material or evolved stars?

Finally, we discuss contamination of objects that are photo-ionized by non-AGN sources. Most of the identified AGNs are low-luminosity, low-ionization objects (LINERs: Heckman 1980) as quantified in Paper-II and there are several possible origins of LINER-like spectra: low-ionization AGNs (Ho et al. 1993; Ho et al. 1997), shocks due to supernova/jets (Cox 1972; Heckman 1980; Dopita & Sutherland 1995; Dopita & Sutherland 1996), Wolf-Rayet stars (Terlevich & Melnick 1985; Kewley et al. 2001), post-starburst (Taniguchi et al. 2000), and post-AGB stars (Binette et al. 1994; Stasińska et al. 2008; Sarzi et al. 2010; Cid Fernandes et al. 2011). LINERs likely constitute a heterogeneous class of objects (Ho 2008). The existence of broad permitted lines in a fraction of LINERs provides strong evidence for the AGN origin (Ho et al. 1993; Ho et al. 1997), but relative contributions of the other ionizing mechanisms to the overall LINER population remain unclear.

Let us focus on the O+Bn class, in which more than 60% of the Oxygen-excess objects fall. These objects show only weak emission lines and therefore their underlying star formation activities are weak (otherwise we would have observed strong emission lines). For such objects, we can reject Wolf-Rayet stars and supernova as a primary cause of the Oxygen flux excess because these sources play a role only in star forming galaxies. The post-starburst origin is unlikely to produce such a large number of AGNs and unlikely a primary cause, too. Cid Fernandes et al. (2011) suggest that galaxies with

$EW(H\alpha) < 3\text{\AA}$  are likely due to post-AGB stars based on a photo-ionization calculation of a single burst stellar population. We find that a significant fraction (75%) of O+Bn objects have  $EW(H\alpha) < 3\text{\AA}$ . But, we argue that many of them are actually AGNs. We find that two-thirds of O+Bn objects detected in X-rays (excluding those in the dashed region of Fig. 11) have  $EW(H\alpha) < 3\text{\AA}$ . We obtain a fairly similar number for those detected in radio (67%; again, those dominated by star formation are excluded from the statistics). Recently, Capetti & Baldi (2011) also reported on a radio detection of quiescent galaxies in SDSS. These X-ray and radio detected sources are probably real AGNs and this suggests that  $EW(H\alpha) < 3\text{\AA}$  does not necessarily mean that the observed Oxygen-excess is due to post-AGB stars. The fact that a fraction of OnBn objects are detected in radios (Table 2) adds a further line of argument against  $EW(H\alpha) < 3\text{\AA}$ .

However, recent integral spectroscopy of nearby galaxies has revealed diffuse extended emission in early-type galaxies and seem to provide evidence of contributions from post-AGB stars. Sarzi et al. (2010) observed that nearby early-type galaxies with radio detections show extended emission. These galaxies show LINER-like emission line ratios and Sarzi et al. (2010) suggested that post-AGB stars can supply enough ionizing photons to explain the observation and thus the photo-ionization is primarily due to post-AGB stars. However, an uncertainty in the fraction of ionizing photons that are reprocessed into emission and our limited understanding of the last stage of the stellar evolution seem to hamper a firm conclusion. Extended line emission is also recently observed by Yan & Blanton (2011). They claimed that the ionizing parameter increases towards larger radii from the galaxy center and the most natural explanation of it would be due to post-AGB stars, although they found that post-AGB stars cannot supply enough ionizing photons. One can turn the question around and ask whether AGN can supply enough photons to explain the observed emission lines. Maoz et al. (1998) and Eracleous et al. (2010b) reported that a fraction of LINERs show a severe deficit of ionizing photons and need other ionization sources. From these observations, there is no doubt that the Oxygen-excess objects are contaminated by the non-AGN emission and at least a fraction of observed emission line luminosities is likely due to post-AGB stars.

However, the contributions from post-AGB stars may not be very significant. We will discuss in depth in Section 3.3 of Paper-II, but we briefly outline our argument here. We observe a clear correlation between optical emission line luminosities and hard X-ray luminosities (Fig 3 of Paper-II). Post-AGB stars are not luminous in hard X-rays and the hard X-ray luminosity is a good measure of AGN activity. On the other hand, optical emission lines can be significantly contaminated by post-AGB photo-ionization. The observed clear correlation suggests that the contribution from post-AGB stars to the observed optical emission is not severe. The hard X-ray detected sources have typical properties of the Oxygen-excess objects (they have stellar mass of  $> 10^{10}$  and are mostly red galaxies with low SFRs of  $< 0.1M_{\odot} \text{ yr}^{-1}$ ), thus they represent the Oxygen-excess objects well. One might worry that non-AGN sources such as low-mass X-ray binaries may be contributing to the observed X-rays because these binaries often significantly contribute to

the overall X-ray emission in massive quiescent galaxies. But, we show in Fig. 5 of Paper-II that the hard X-ray luminosity does not correlate with stellar mass. The rather weak dependence of X-ray luminosity on the host galaxy mass is also observed by other authors (Mullaney et al. 2012; Aird et al. 2011). This excludes the low-mass X-ray binary origin of the observed X-rays because their contribution should increase with increasing stellar mass (Kim & Fabbiano 2004). The most likely origin of the hard X-ray is therefore AGN and the clear correlation between hard X-ray and optical luminosity shown in Paper-II suggests that the contamination from post-AGB stars to the observed emission line is not significant.

The X-ray sample is a just small portion of the entire Oxygen-excess objects. We make another subsample of them to further quantify the role of post-AGB stars. This is a subsample of quiescent (i.e., SFR is zero) Oxygen-excess objects in a narrow redshift slice to eliminate any redshift effects. The emission due to post-AGB stars should correlate strongly with stellar mass contained within the area covered by the fibers, while the AGN emission is unlikely to be strongly correlated with mass (Aird et al. 2011; Mullaney et al. 2012). Within the narrow redshift slice, we find that observed emission line luminosities only weakly depend on stellar mass, which suggests that post-AGB stars do not significantly contribute to the overall emission. Based on a very simple model, we find that 23% of the emission is due to post-AGB stars in typical Oxygen-excess objects with stellar mass of  $10^{10} M_{\odot}$  within the fibers.

It seems that a large fraction of O+Bn objects are likely AGNs. But, we still do not know the exact abundance of non-AGNs and the exact fractional contribution of the post-AGB photo-ionization to the observed emission line luminosities. We may well have Oxygen-excess objects whose emission is completely powered by post-AGB stars. It has been a challenging task to pin down the abundance of true/false AGNs (Ho 2008) and this would probably require deep multi-wavelength observations of the nuclear region of well defined sample of galaxies. The SDSS fibers subtend 3 arcsec on the sky and they include a substantial fraction of bulge and disk components under the typical seeing conditions of the site ( $\sim 1.5$  arcsec). We deem that the SDSS data are not suited to address the issue in depth. Also, our poor understanding of the last phase of the stellar evolution puts further limit on our ability to constrain the role of post-AGB stars. For these reasons, we do not try to go further from here. This unknown fraction of contaminating non-AGNs (although it will be small) remains one of the major uncertainties in results presented in Paper-II and a more detailed study of both observational and theoretical aspects would be needed to put a more stringent constraint on the role of non-AGN photo-ionization.

#### 4. Summary

We have developed a novel technique to identify AGNs based on a very simple idea of comparing expected and observed emission line luminosities. We perform a spectral fits of the SDSS galaxies to obtain SFRs and dust extinction, from which we can compute expected emission line luminosities due to star formation. By comparing the expected luminosities with observed luminosities, we can statistically identify AGNs. In

this comparison, we use  $[\text{OII}]+[\text{OIII}]$  luminosities. This choice is motivated by the fact that AGNs span a wide range in ionization state as quantified in Paper-II.

To test the newly developed method, we have made extensive comparisons with the other AGN identification methods, namely, BPT, X-rays and radio. Our method suffers from contamination and incompleteness as all the other methods do. But, the average properties from the stacked spectra and the detection rates of X-ray and radio sources all suggest that the Oxygen-excess method is a good statistical method to identify AGNs. The most unique feature of the method is its sensitivity. We have demonstrated that our method is applicable to  $\sim 80\%$  of the galaxies, while BPT can be applied to only  $\sim 40\%$ . All the analyses above show that the Oxygen-excess method works fairly well in identifying such low-luminosity objects. Another very unique feature, which we have not emphasized in this paper, is its capability to subtract star formation component from the observed emission line luminosity to extract pure AGN emission, which is crucial to characterize AGN activities. We will make an extensive use of these features to study the nature of low-luminosity AGNs in Paper-II.

To summarize, the strengths and weaknesses of our method would be:

#### STRENGTHS:

- It requires only a sum of  $[\text{OII}]$  and  $[\text{OIII}]$ . Note that the BPT diagnostics requires 4 lines and it takes ratios of the lines, meaning that one needs to detect each line at a sufficiently significant level.  $\text{H}\beta$  is often the weakest line in AGNs and that limits the sensitivity of BPT.
- It does not require  $\text{H}\alpha$ , allowing us to go up to  $z \sim 1$  with optical spectrographs. If one uses  $[\text{OII}]$  only at a risk of missing high ionization AGNs, one can go up to even higher redshifts of  $z \sim 1.7$ .
- It is fairly sensitive to low-luminosity AGNs that cannot be identified by the BPT diagnostics.
- It is able to subtract emission line fluxes due to star formation and extract AGN fluxes. We will make a full use of this feature in Paper-II.

#### WEAKNESSES:

- It requires a robust continuum detection in well-calibrated spectra (i.e., this method is applicable only to bright galaxies). But, we deem that multi-wavelength photometry could be used when continuum spectra are not available.
- It misses a fraction of AGNs selected from the BPT diagnostics, X-rays, and radio.
- It suffers from contamination of star forming galaxies. But, as emphasized throughout this paper, all methods suffer from incompleteness and contamination.
- It misses weak AGNs in actively star forming galaxies as we will fully quantify in Paper-II.

We would like to thank Masataka Fukugita and John Silverman for extensive discussions, Luis Ho, Toru Nagao, and Yoshihiro Ueda, for useful conversations, Naoki Yasuda for providing the computing environment, and Yen-Ting Lin for helpful comments on the paper. This work was supported

by World Premier International Research Center Initiative (WPI Initiative), MEXT, Japan and in part by KAKENHI No. 23740144. This research has made use of data obtained from the Chandra Source Catalog, provided by the Chandra X-ray Center (CXC) as part of the Chandra Data Archive. We thank the anonymous referee for his/her useful comments, which helped improve the paper.

Funding for the Sloan Digital Sky Survey (SDSS) and SDSS-II has been provided by the Alfred P. Sloan Foundation, the Participating Institutions, the National Science Foundation, the U.S. Department of Energy, the National Aeronautics and Space Administration, the Japanese Monbukagakusho, and the Max Planck Society, and the Higher Education Funding Council for England. The SDSS Web site is <http://www.sdss.org/>.

The SDSS is managed by the Astrophysical Research Consortium (ARC) for the Participating Institutions. The Participating Institutions are the American Museum of Natural History, Astrophysical Institute Potsdam, University of Basel, University of Cambridge, Case Western Reserve University, The University of Chicago, Drexel University, Fermilab, the Institute for Advanced Study, the Japan Participation Group, The Johns Hopkins University, the Joint Institute for Nuclear Astrophysics, the Kavli Institute for Particle Astrophysics and Cosmology, the Korean Scientist Group, the Chinese Academy of Sciences (LAMOST), Los Alamos National Laboratory, the Max-Planck-Institute for Astronomy (MPIA), the Max-Planck-Institute for Astrophysics (MPA), New Mexico State University, Ohio State University, University of Pittsburgh, University of Portsmouth, Princeton University, the United States Naval Observatory, and the University of Washington.

#### Appendix 1. Extinction law and non-solar metallicity models

In this appendix, we justify the choice of the Cardelli et al. (1989) extinction curve over the Charlot & Fall (2000) curve. We also justify the exclusion of non-solar metallicity models.

The reason why we prefer the Cardelli et al. (1989) curve is because it gives better agreement between SFRs from the spectral fits and those from  $\text{H}\alpha$  corrected for the extinction. As shown in the left plot of Fig. 1, our SFR estimates are reasonably accurate, although there is a tilt. This tilt becomes slightly larger if we adopt the Charlot & Fall (2000) extinction curve as shown in Fig. 14. Also, the mean offset between SFRs from the spectral fits and those from  $\text{H}\alpha$  and  $\text{H}\beta$  increases. Furthermore, we find that the discrepancy between the dust extinctions from the fits and those from the balmer decrement becomes larger if we use Charlot & Fall (2000). Because we extensively use SFRs and dust estimates from the spectral fits, we prefer to use the Cardelli et al. (1989) extinction curve to obtain better SFRs and dust estimates. It might appear at odds to change only the extinction curve of Charlot & Fall (2000), while keeping the two component dust model unchanged. But, the two component model is physically sensible and the observed better agreement with SFRs and dust justifies the modification of the extinction curve. We further note that Charlot & Fall (2000) calibrated their model parameters using starburst galaxies, but a very small portion of our sample is undergoing such activ-



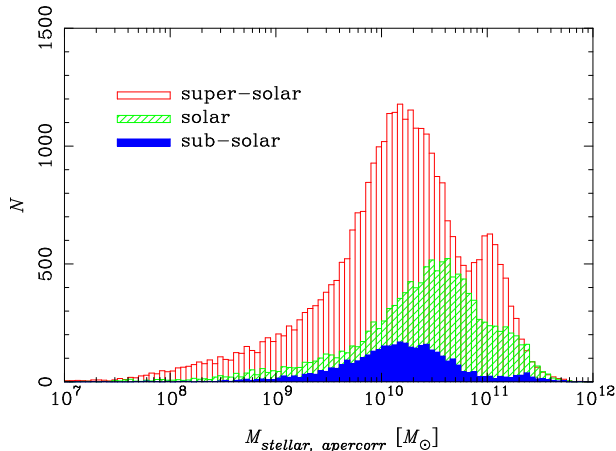


**Fig. 15.** Stellar mass distributions. The open, shaded, and filled histograms show galaxies fit with super-solar, solar, and sub-solar metallicity models, respectively.

ities. It is interesting note that we can predict emission line fluxes equally well even if we adopt the Charlot & Fall (2000) model. It is likely due to the degeneracies between SFR and dust extinction

Next, we turn to the metallicity dependence of our model fits. We generate the model templates with super-solar, solar, and sub-solar metallicities and perform the spectral fits using all the templates. Fig. 15 shows the distribution of stellar mass of galaxies. Our model fits do not reproduce the mass-metallicity relation (more massive galaxies are more metal-rich, e.g., Nelan et al. 2005), but the stellar mass distributions in Fig. 15 do not show any strong dependence of stellar mass on metallicity. Fig. 15 shows that we cannot estimate metallicity of galaxies from our spectral fits. This would not be too surprising because metallicity estimates require careful absorption line diagnostics to break the age-metallicity degeneracy (Worthey 1994). Furthermore, sub/super solar metallicity models degrade the accuracy of our emission line flux estimates (a significant amount of galaxies have  $H\alpha/H\beta < 2.86$ ) due to inaccurate corrections for stellar absorption. For these reasons, we use only the solar metallicity models in our spectral analyses. We note that Asari et al. (2007) obtained a correlation between stellar metallicity and gas-phase metallicity from versatile spectral fits albeit with a significant scatter.

## Appendix 2. Veilleux & Osterbrock diagrams

Veilleux & Osterbrock (1987) extended the commonly used BPT diagnostics and showed that the [OI] and [SII] lines are also sensitive to the presence of AGNs. We have made extensive comparisons between the Oxygen-excess and BPT diagnostics, but here we make further comparisons with the Oxygen-excess and Veilleux & Osterbrock (1987) diagrams.

We present the distributions of Oxygen-excess on the Veilleux & Osterbrock (1987) diagrams in Figs. 16 and 17. The distributions of all galaxies do not show a clear branch of AGNs like the one seen in Fig. 6. As mentioned in the main body of the paper, the clear AGN sequence in the BPT diagram is likely due to the secondary nature of nitrogen. Theoretical

modeling of the Veilleux & Osterbrock (1987) diagrams shows a strong overlap between star forming galaxies and AGNs on these diagrams (Stasińska et al. 2006). In fact, the Oxygen-excess objects spread over both the star forming and AGN regions of the diagrams.

Fig. 18 shows the locations of the stacked objects on the Veilleux & Osterbrock (1987) diagrams. The trend is similar to what observed in the BPT diagram (Fig. 8), albeit with a larger degeneracy between star forming galaxies and AGNs. On these diagrams, only O+B+, O+Bn, and OnBn are clearly in the AGN region. The other classes are fairly close to each other and are all in the star forming region. But, as mentioned above, this does not necessarily mean that they do not host AGNs because the star forming sequence and AGN sequence overlap on these diagrams.

The distribution of X-ray objects is shown in Fig. 19. Many of the sources are in the AGN region of the diagram, but a fraction of AGNs is scattered to the star forming region. This may appear in contrast to the BPT diagram in Fig. 10, where we have observed that most X-ray sources are in the AGN region of the diagram. Radio sources are shown in Fig. 20. The radio objects spread over the diagram, but objects that do not show any Oxygen excess tend to lie at the bottom-left tip of the star forming sequence. These objects are likely actively forming stars and the radio emission is due to star formation.

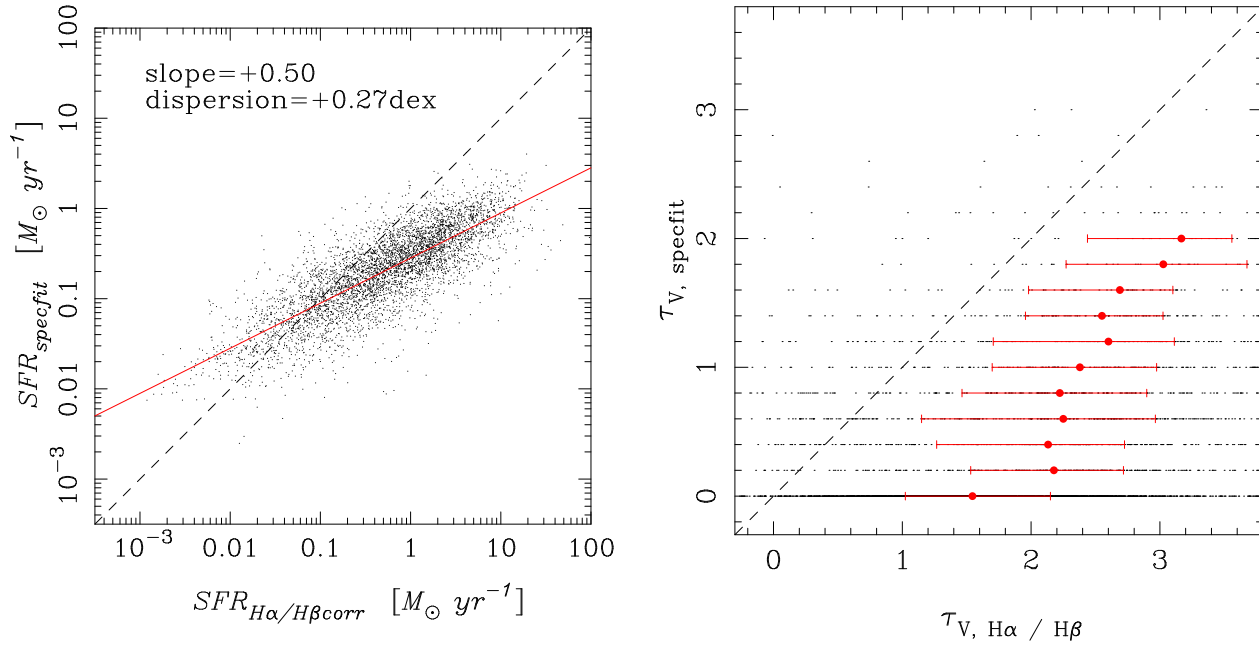
Overall, the Veilleux & Osterbrock (1987) diagrams show consistent results with BPT, although their sensitivity to intermediate classes is limited. As discussed in the main body of the paper, most of the Oxygen-excess objects are in the O+Bn class and the figures presented in this appendix show that O+Bn objects are clearly in the AGN region of the diagrams. This adds further evidence that most of the Oxygen-excess method works fairly well in identifying AGNs.

## Appendix 3. Host galaxy properties of O-B+ objects

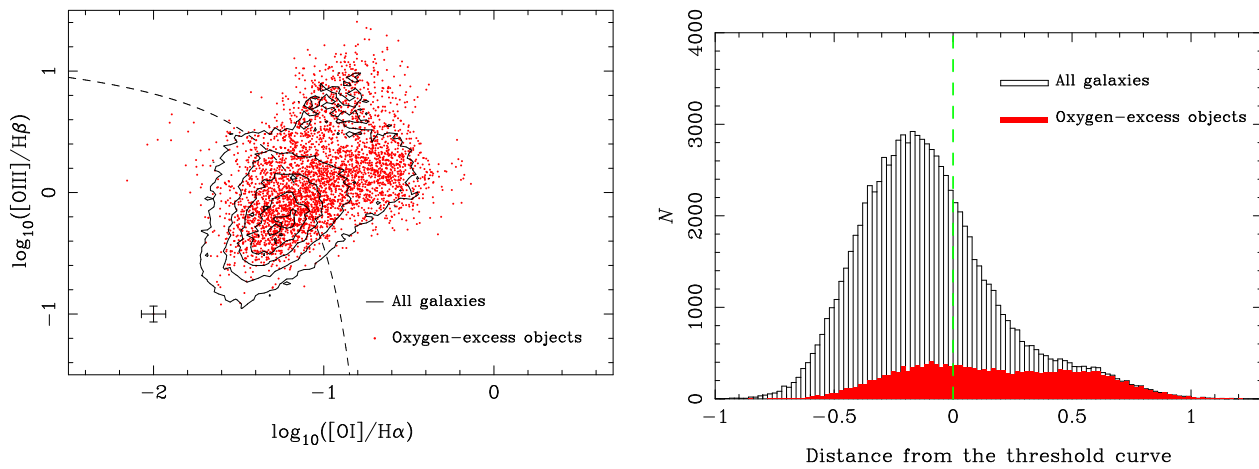
The Oxygen-excess method misses a fraction of BPT AGNs (O-B+) due possibly to active underlying star formation. It could also be due to strong featureless continuum from AGN, which affects our SFR estimates. We cannot easily distinguish these two possibilities as discussed in the main body of the paper. We thus do not try to characterize their AGN activities and host galaxy SFRs. Instead, we quantify their stellar mass, color, and morphological types of the hosts and show that these missing AGNs do not change our conclusions in Paper-II.

Fig. 21 shows the O-B+ fraction as a function of stellar mass of the host galaxies. The O-B+ objects typically have  $10^{10-11} M_{\odot}$  and the fraction is low at the most massive and least massive ends. As we show in Paper-II, the fraction of the Oxygen-excess objects is nearly 60% at  $10^{11} M_{\odot}$ . The fraction of the missing AGNs is an order of magnitude lower and they do not affect our results in any significant way.

We plot the color and morphology distribution in Fig. 22. As detailed in Section 4 of Paper-II, the color is  $k$ -corrected rest-frame  $u-r$  color and the morphology is characterized with the inverse concentration index (Shimasaku et al. 2001; Strateva et al. 2001) measured in the  $z$ -band. The O-B+ objects tend to have intermediate color and morphological types, which is similar to the overall properties of the BPT AGNs (see paper-



**Fig. 14.** As in Fig. 1, but here we assume the Charlot & Fall (2000) extinction curve. Plotted are a small subset ( $\sim 20,500$  objects) of the entire sample.



**Fig. 16.** Same as in Fig. 6, but here we use  $[OI]/H\alpha$  in place of  $[NII]/H\alpha$ . The dashed line to separate star forming galaxies from AGNs is from Kewley et al. (2001).

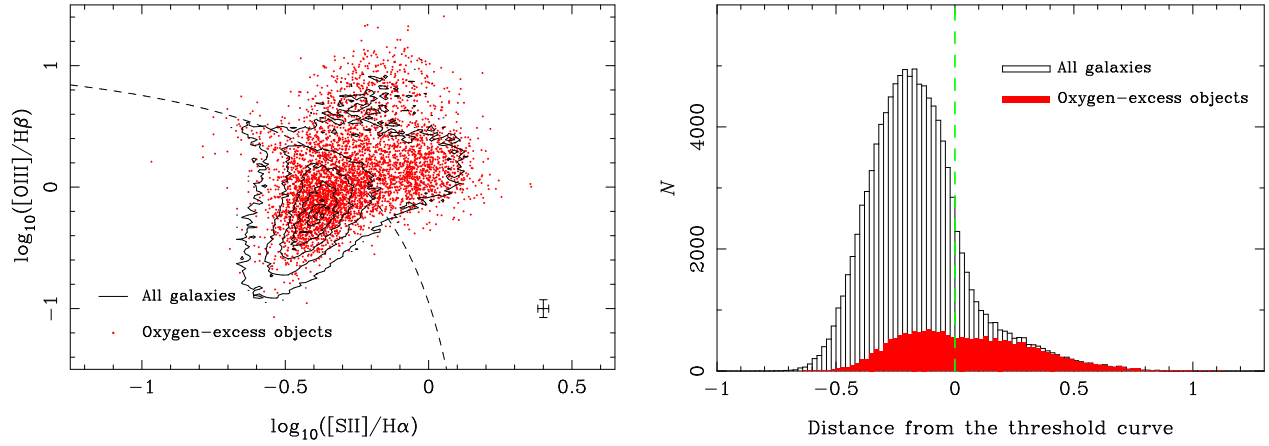


**Fig. 17.** Same as in Fig. 6, but here we use  $[SII]/H\alpha$  in place of  $[NII]/H\alpha$ . The dashed line to separate star forming galaxies from AGNs is from Kewley et al. (2001).

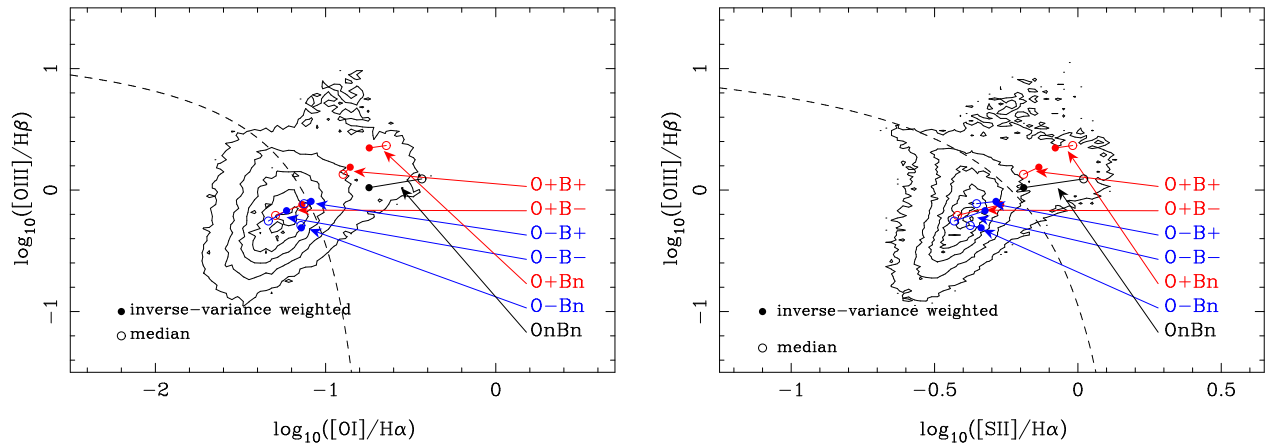


**Fig. 18.** Same as Fig. 8, but for the two Veilleux & Osterbrock (1987) diagrams. The locations of the stacked objects are indicated by the points and arrows. The filled and open circles are measured from the inverse-variance weighted stacking and from the median stacking, respectively.

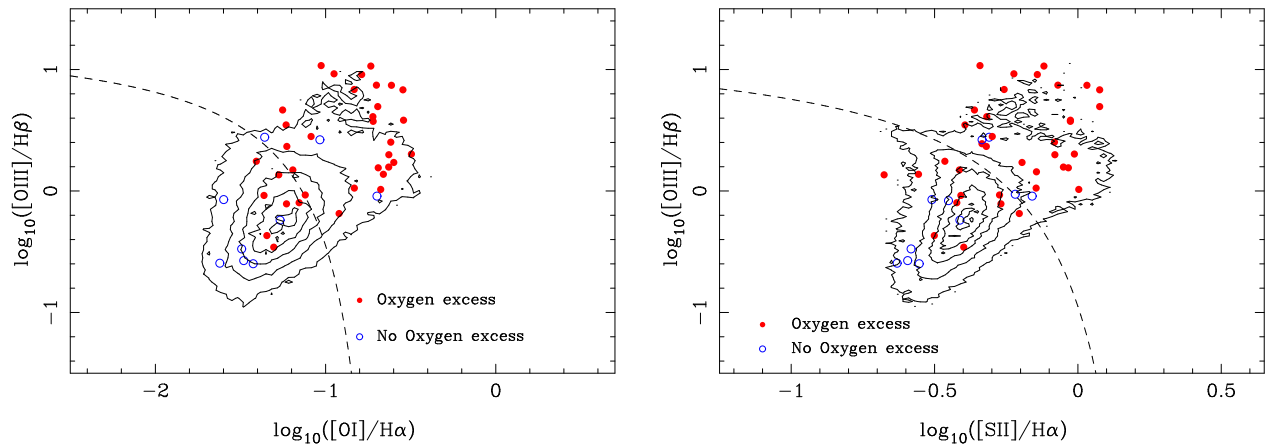


**Fig. 19.** As in Fig. 10, but for the two Veilleux & Osterbrock (1987) diagrams.

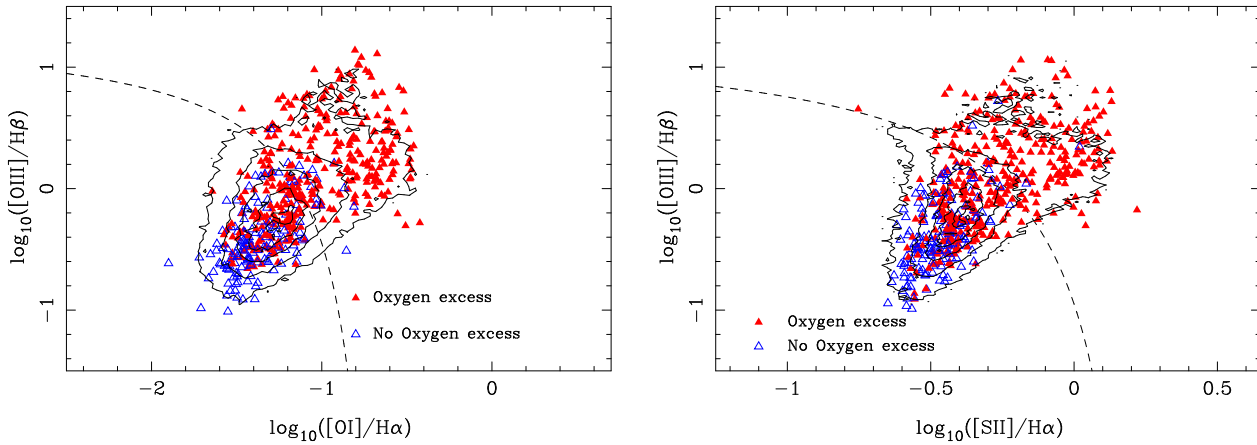


Fig. 20. As in Fig. 12, but for the two Veilleux & Osterbrock (1987) diagrams.

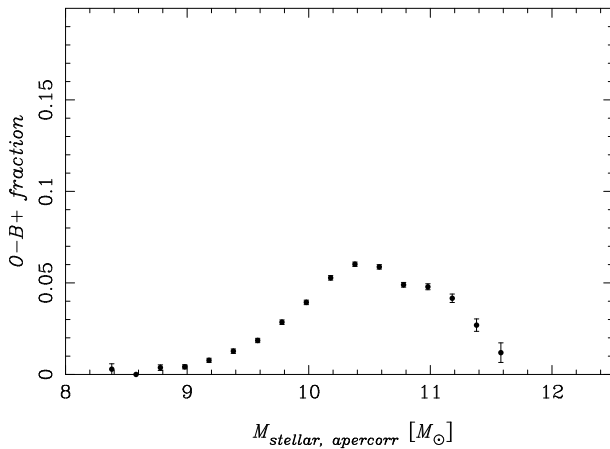


Fig. 21. Fraction of O-B+ objects as a function of stellar mass.

II). They avoid the red sequence, which shows that they are undergoing star formation.

Overall, properties of the O-B+ objects are similar to the BPT AGNs in general. We have confirmed that our conclusions in Paper-II remain unchanged if we include these missing population in the analysis.

## References

- Abazajian, K. N., et al. 2009, *ApJS*, 182, 543  
Aird, J., Coil, A. L., Moustakas, J., et al. 2011, arXiv:1107.4368  
Asari, N. V., Cid Fernandes, R., Stasińska, G., Torres-Papaqui, J. P., Mateus, A., Sodré, L., Schoenell, W., & Gomes, J. M. 2007, *MNRAS*, 381, 263  
Baldwin, J. A., Phillips, M. M., & Terlevich, R. 1981, *PASP*, 93, 5  
Becker, R. H., White, R. L., & Helfand, D. J. 1995, *ApJ*, 450, 559  
Binette, L., Magris, C. G., Stasińska, G., & Bruzual, A. G. 1994, *A&A*, 292, 13  
Bower, R. G., Benson, A. J., Malbon, R., Helly, J. C., Frenk, C. S., Baugh, C. M., Cole, S., & Lacey, C. G. 2006, *MNRAS*, 370, 645  
Bruzual, G., & Charlot, S. 2003, *MNRAS*, 344, 1000  
Capetti, A., & Baldi, R. D. 2011, *A&A*, 529, A126  
Cardelli, J. A., Clayton, G. C., & Mathis, J. S. 1989, *ApJ*, 345, 245  
Chabrier, G. 2003, *PASP*, 115, 763  
Charlot, S., & Fall, S. M. 2000, *ApJ*, 539, 718  
Cid Fernandes, R., Stasińska, G., Mateus, A., & Vale Asari, N. 2011, *MNRAS*, 249  
Colless, M., et al. 2003, arXiv:astro-ph/0306581  
Condon, J. J. 1992, *ARA&A*, 30, 575  
Cox, D. P. 1972, *ApJ*, 178, 143  
Croton, D. J., et al. 2006, *MNRAS*, 365, 11  
Dickey, J. M., & Lockman, F. J. 1990, *ARA&A*, 28, 215  
Doi, M., et al. 2010, *AJ*, 139, 1628  
Dopita, M. A., & Sutherland, R. S. 1995, *ApJ*, 455, 468  
Dopita, M. A., & Sutherland, R. S. 1996, *ApJS*, 102, 161  
Eisenstein, D. J., et al. 2001, *AJ*, 122, 2267  
Eracleous, M., Hwang, J. A., & Flohic, H. M. L. G. 2010a, *ApJS*, 187, 135  
Eracleous, M., Hwang, J. A., & Flohic, H. M. L. G. 2010b, *ApJ*, 711, 796  
Evans, I. N., et al. 2010, *ApJS*, 189, 37  
Ferrarese, L., & Merritt, D. 2000, *ApJL*, 539, L9  
Flohic, H. M. L. G., Eracleous, M., Chartas, G., Shields, J. C., & Moran, E. C. 2006, *ApJ*, 647, 140  
Fukugita, M., Ichikawa, T., Gunn, J. E., Doi, M., Shimasaku, K., & Schneider, D. P. 1996, *AJ*, 111, 1748  
Gebhardt, K., et al. 2000, *ApJL*, 539, L13  
Granato, G. L., De Zotti, G., Silva, L., Bressan, A., & Danese, L. 2004, *ApJ*, 600, 580  
Gunn, J. E., et al. 1998, *AJ*, 116, 3040  
Gunn, J. E., et al. 2006, *AJ*, 131, 2332  
Heckman, T. M. 1980, *A&A*, 87, 152  
Heckman, T. M., Kauffmann, G., Brinchmann, J., Charlot, S., Tremonti, C., & White, S. D. M. 2004, *ApJ*, 613, 109  
Hopkins, A. M., et al. 2003, *ApJ*, 599, 971  
Ho, L. C., Filippenko, A. V., & Sargent, W. L. W. 1993, *ApJ*, 417, 63  
Ho, L. C., Filippenko, A. V., & Sargent, W. L. W. 1995, *ApJS*, 98, 477  
Ho, L. C., Filippenko, A. V., Sargent, W. L. W., & Peng, C. Y. 1997, *ApJS*, 112, 391  
Ho, L. C. 2008, *ARA&A*, 46, 475  
Irwin, J. A., Athey, A. E., & Bregman, J. N. 2003, *ApJ*, 587, 356  
Ivezić, Ž., et al. 2007, *AJ*, 134, 973  
Juneau, S., Dickinson, M., Alexander, D. M., & Salim, S. 2011, *ApJ*, 736, 104  
Kauffmann, G., et al. 2003, *MNRAS*, 346, 1055  
Kennicutt, R. C., Jr. 1998, *ARA&A*, 36, 189  
Kewley, L. J., Dopita, M. A., Sutherland, R. S., Heisler, C. A., & Trevena, J. 2001, *ApJ*, 556, 121  
Kewley, L. J., & Dopita, M. A. 2002, *ApJS*, 142, 35

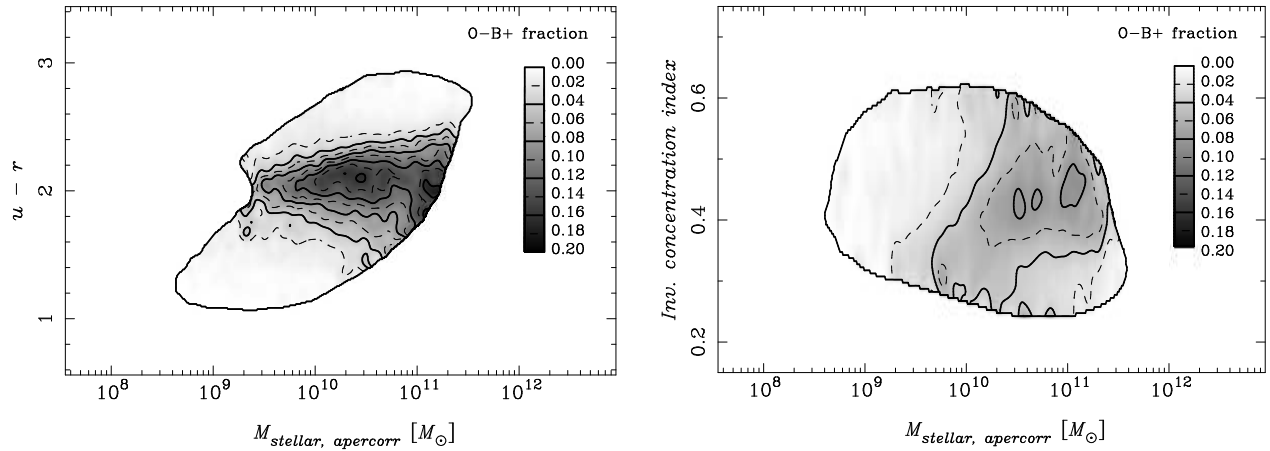


**Fig. 22.** O-B+ fraction as functions of rest-frame  $u - r$  color and stellar mass (left), and inverse concentration index and stellar mass (right). Note that the contours are drawn at lower levels than those in Paper-II to clarify the distribution of the O-B+ objects.

- Kewley, L. J., Groves, B., Kauffmann, G., & Heckman, T. 2006, *MNRAS*, 372, 961
- Kormendy, J., & Richstone, D. 1995, *ARA&A*, 33, 581
- Lamareille, F., Mouhcine, M., Contini, T., Lewis, I., & Maddox, S. 2004, *MNRAS*, 350, 396
- Lin, Y.-T., Shen, Y., Strauss, M. A., Richards, G. T., & Lunnan, R. 2010, *ApJ*, 723, 1119
- Kim, D.-W., & Fabbiano, G. 2004, *ApJ*, 611, 846
- Kinney, A. L., Antonucci, R. R. J., Ward, M. J., Wilson, A. S., & Whittle, M. 1991, *ApJ*, 377, 100
- Magorrian, J., et al. 1998, *AJ*, 115, 2285
- Mainieri, V., Hasinger, G., Cappelluti, N., et al. 2007, *ApJS*, 172, 368
- Maoz, D., Koratkar, A., Shields, J. C., Ho, L. C., Filippenko, A. V., & Sternberg, A. 1998, *AJ*, 116, 55
- Miley, G., & De Breuck, C. 2008, *A&A Rev.*, 15, 67
- Morrison, R., & McCammon, D. 1983, *ApJ*, 270, 119
- Mullaney, J. R., Pannella, M., Daddi, E., et al. 2012, *MNRAS*, 419, 95
- Nelan, J. E., Smith, R. J., Hudson, M. J., Wegner, G. A., Lucey, J. R., Moore, S. A. W., Quinney, S. J., & Suntzeff, N. B. 2005, *ApJ*, 632, 137
- Osterbrock, D. E., & Ferland, G. J., 2006, *Astrophysics of Gaseous Nebulae and Active Galactic Nuclei*, Second Edition, University Science Books
- Padmanabhan, N., et al. 2008, *ApJ*, 674, 1217
- Richards, G. T., et al. 2002, *AJ*, 123, 2945
- Rola, C. S., Terlevich, E., & Terlevich, R. J. 1997, *MNRAS*, 289, 419
- Sarzi, M., Shields, J. C., Schawinski, K., et al. 2010, *MNRAS*, 402, 2187
- Schawinski, K., Thomas, D., Sarzi, M., Maraston, C., Kaviraj, S., Joo, S.-J., Yi, S. K., & Silk, J. 2007, *MNRAS*, 382, 1415
- Schlegel, D. J., Finkbeiner, D. P., & Davis, M. 1998, *ApJ*, 500, 525
- Schmitt, H. R., Storchi-Bergmann, T., & Cid Fernandes, R. 1999, *MNRAS*, 303, 173
- Seyfert, C. K. 1943, *ApJ*, 97, 28
- Shimasaku, K., et al. 2001, *AJ*, 122, 1238
- Stasińska, G., Cid Fernandes, R., Mateus, A., Sodr e, L., & Asari, N. V. 2006, *MNRAS*, 371, 972
- Stasińska, G., Vale Asari, N., Cid Fernandes, R., Gomes, J. M., Schlickmann, M., Mateus, A., Schoenell, W., & Sodr e, L., Jr. 2008, *MNRAS*, 391, L29
- Strateva, I., et al. 2001, *AJ*, 122, 1861
- Strauss, M. A., et al. 2002, *AJ*, 124, 1810
- Tanaka, M., PASJ, in press (Paper-II)
- Taniguchi, Y., Shioya, Y., & Murayama, T. 2000, *AJ*, 120, 1265
- Terlevich, R., & Melnick, J. 1985, *MNRAS*, 213, 841
- Tojeiro, R., Percival, W. J., Heavens, A. F., & Jimenez, R. 2011, *MNRAS*, 413, 434
- Tremonti, C. A., et al. 2004, *ApJ*, 613, 898
- Veilleux, S., & Osterbrock, D. E. 1987, *ApJS*, 63, 295
- Watson, M. G., et al. 2009, *A&A*, 493, 339
- White, R. L., Becker, R. H., Helfand, D. J., & Gregg, M. D. 1997, *ApJ*, 475, 479
- Worthey, G. 1994, *ApJS*, 95, 107
- Yan, R., Newman, J. A., Faber, S. M., Konidaris, N., Koo, D., & Davis, M. 2006, *ApJ*, 648, 281
- Yan, R., et al. 2011, *ApJ*, 728, 38
- Yan, R., & Blanton, M. R. 2011, arXiv:1109.1280
- York, D. G., et al. 2000, *AJ*, 120, 1579